Thermal Scanning Probe Lithography for 2D Materials

Master of Science (MSc)

Yacine Benkirane

Under the Supervision of Dr. Peter Grütter

at the McGill University Department of Physics

June 2024

A thesis submitted to McGill University in partial fulfillment of the requirements for the degree of Master of Science

ACKNOWLEDGEMENTS

I would like to thank my supervisor and mentor - Prof. Peter Grütter - for giving me this amazing opportunity to work on the unique Nanofrazor Explore t-SPL instrument and altogether encourage me to purse my passions in life. I am extremely grateful for his unique guidance and enthusiasm.

My sincere thanks to Dr. Zhao Lu and all lab-technicians for their expertise and patience in repairing our cleanroom facilities. I also could not have done it without Robert Gagnon's dedication and guidance.

Many thanks to Profs. Kai Wang, Guillaume Gervais, and Michael Hilke for the insightful and exciting CMX discussions.

A loving "Thank you!" to the two-to-three generations of Grütter Group members I've had the pleasure of meeting, full of inspirational and friendly conversations as well as energizing chess games. Finally, thank you to my family for your love and support ...

Contents

List of Figures

ABSTRACT

The fabrication of semiconducting devices using mechanically-exfoliated monolayers presents significant challenges, primarily due to the difficulty in identifying and characterizing the target monolayer, substantial surface inhomogeneities and adhesives, and invasive fabrication methods. This thesis aims to develop a reproducible methodology for the non-invasive fabrication of nanoscale-contacts on mechanically exfoliated two-dimensional semiconductor sheets through thermal scanning probe lithography (t-SPL). Our approach leverages a bilayer liftoff (BLO) process employing polydimethylglutarimide (PMGI) and polyphthalaldehyde (PPA) resists, integrated with a combination of t-SPL and UV-laser lithography techniques, to fabricate a multitude of model electrical transport measurement architectures (four point probe, van der Pauw, etc). In this work, we study important steps and critical issues encountered during both the classification and fabrication of these 2D devices. We provide a guide to overcoming common - yet previously unexamined - flaws in the t-SPL nanofabrication of 2DM devices such as the correction of capillary force-induced resist torsion by adjusting spin coating parameters. The consequences of over-development during wet-etching and under-dosing during UV lithography are additionally discussed.

RÉSUMÉ

La fabrication de dispositifs semi-conducteurs à l'aide de monocouches exfoliées mécaniquement présente des défis significatifs, principalement en raison de la difficulté d'identifier et de caractériser la monocouche cible, des inhomogénéités de surface substantielles et des adhésifs, ainsi que des méthodes de fabrication invasives. Cette thèse vise à développer une méthodologie reproductible pour la fabrication non invasive de contacts à l'échelle nanométrique sur des feuilles de semi-conducteurs bidimensionnelles exfoliées mécaniquement, grâce à la lithographie par sonde thermique (t-SPL). Notre approche exploite un processus de levée bilaminaire (BLO) utilisant des résines de polydiméthylglutarimide (PMGI) et de polyphthalaldéhyde (PPA), intégré à une combinaison de techniques de t-SPL et de lithographie laser UV, pour fabriquer une multitude d'architectures modèles de mesure de transport électrique (sonde à quatre points, van der Pauw, etc.). Dans cette these, nous étudions les étapes importantes et les problèmes critiques rencontrés lors de la classification et de la fabrication de ces dispositifs 2D. Nous fournissons un guide pour surmonter les défauts courants - mais jusqu'à présent non examinés - dans la nanofabrication t-SPL des dispositifs 2DM, tels que la correction de la torsion des résines induite par les forces capillaires en ajustant les paramètres de centrifugation. Les conséquences du surdéveloppement lors de la gravure humide et du sous-dosage lors de la lithographie UV sont également discutées.

1 INTRODUCTION

Richard P. Feynman's 1959 talk "There is **Plenty** of Room at the Bottom" and Gordon E. Moore's 1965 paper "Cramming more components onto integrated circuits" are excellent examples of the predictions, ambitions, and concerns held at the beginning of the semiconductor industry [Feynman, 1959; Moore, 1965]. It was well-understood then that devices such as transistors, photoelectric detectors and engineered bits of information or metamaterials would improve in cost and resolution at an exponential rate. Through their understanding of semiconductor physics, they could dream of automatic controls for automobiles, near-atomic-scale electric motors, miniature home computers, and personal telecommunication devices. These inspirational invitations to all curious minds laid the foundations for nanotechnology as we know it today.

We are now at the start of the *Data Age*: data-driven technologies span every aspect of our lives from transportation and healthcare to communication and energy production. With the increasing functional density of integrated circuits comes the heat death of components, device volatility, and enormous heat generation. Cloud computing, machine learning training and inference, cryptocurrency mining, and entertainment server farms consume colossal amounts of energy. Although "hyperscale" data centres like those maintained by Nvidia, Amazon, Meta, and Alphabet are able to considerably offset their carbon footprints through sustainable wind and solar infrastructure, much of the industry follows less optimal thermodynamic practices.

In 2022, data centre electricity consumption for computation and cooling was estimated to be 240 - 340 terawatt-hours (TWh), equating roughly one percent of the global energy demand [Malmodin *et al.*, 2023]. Additionally, the public-domain Cambridge Bitcoin Electric-

ity Consumption Index (CBECI) research indicates that bitcoin mining consumes roughly 80 TWh/year and has cumulatively reached 600 TWh in consumption since its inception. The Moroccan molten-salt Ouarzazate Solar Complex, also known as the Noor Power Station, outputs roughly 1.2 TWh/year over 24,000 square kilometers facility [ITA, 2024]. At a similar efficiency, cloud and data mining demands today would require a complex with a surface area roughly the size of Jamaica or Lebanon. Alternatively, this demand would require around 450 single-generator nuclear power plants operating continuously [EIA, 2019]. As user consumption grows exponentially, the United Nations Environment Programme's 2022 Emissions Gap Report predicts that global temperatures may consequently rise by 2.6 $^{\circ}C$ by the end of this century [UNEP, 2022].

As such, there comes a necessity for innovation in novel quantum devices for transfer thermoelectrics, optoelectronics, information storage, and computing architectures. As we follow the path of rational design to drive Moore's Law and fabricate denser, faster, and more reliable components with heterostructured two-dimensional (2D) materials, strongly-correlated electron cross-layer and interface phenomena arise, allowing for the delicate tunability of device properties. This has motivated the research direction of this thesis in developing methodology for non-invasive nanofabrication of metallic patterns and low-contact resistance metal-seminconductor junctions in 2D devices. This introduction serves as an overview of the currently available scanning-type nanofabrication tools at the disposal of the 2D endeavour, their inherent strengths and limitations, as well as the underlying physics that defines these benchmarking metrics.

Currently, capital and operating costs for clean-room lab facilities and mask-less nanolithography technologies are expensive and limited, setting boundaries on progress made in the semiconductor, integrated-circuit (IC), and nanoelectromechanical system (NEMS) industries. For various reasons ranging from cost and scalability to chemical compatibility and resolution limits, substantial efforts both in academic research and industrial applications are being employed to develop means of mask-less nanolithography. This form of nanofabrication can be split into two distinct classifications: scanning beam and scanning probe technologies.

1.1 Scanning Beam Techniques

1.1.1 Electronic

The most common and widely used mask-less technology in top-down nanofabrication is **Electron-Beam Lithography** (EBL), which involves the modification of materials to a substrate using an incident beam of electrons. The technique itself has been cemented into the semiconductor industry and research environment for over 60 years. The ability to easily and inexpensively convert a standard scanning electron microscope (SEM) or scanning transmission electron microscope (STEM) into an EBL tool has also made this a household instrument for academia. The small wavelength of electrons (on the order of 0.1 nm for 10-50 keV electrons) allows for some of the smallest features possible, limited by aberrations, resist mechanical stability, scattering/back-scattering effects, and development due to material properties of the polymers and substrates used in the process. **Resists** are sensitive materials, commonly polymers, which cross-link during exposure; the types and number of polymer layers used in a process can be critical to the resolution, fabrication speed, and overall quality of the device. The intensity and method of modification can be tuned by changing the e-beam dosage and resist type.

The use of a positive resist indicates that only the exposed region is removed from the layer in the end-product; whereas, a negative resist indicates that the exposed region remains at the end of the fabrication process. The most common resists used in EBL are variations of the positive poly-methyl methacrylate (PMMA) and negative epoxy-based SU-8 resists. A massive variety of chemically amplified polymers have been developed for high-speed EBL with chemical modifications occurring at sufficiently low doses (around 30 $\mu C/cm^2$ or 2 electrons per nm^2). The concept of chemical amplification originates from Ito, Willson, and Frechet (1982) at IBM and quickly applied to the manufacturing of dynamic random access memory by deep-UV lithography. The basic working principle dictates that irradiance generates a catalytic species that induces a chain-reaction of chemical transformations, enabling a gain mechanism.

The original scheme is made up of three distinct acid-catalyzed systems: self-developing positive imaging with **depolymerization**, dual-tone (positive or negative) polarity change imaging from **deprotection** of pendant groups, and negative imaging from the **cross-linking** or ring-opening polymerization of pendant epoxide groups. Throughout the years, these mechanisms have been refined and tuned in various ways such as the usage of new acid generators for sensitivity control, the addition of aqueous-base development for semiconductor lithography [Conley *et al.*, 1990] and a switch from self-development to thermal development in PPA to eliminate contamination of tools [Ito, Ueda, and Schwalm, 1988]. The

Primarily due to resist mechanisms and scattering effects, EBL products have generally been limited to 4 *nm* features and 8 *nm* half-pitch using "traditional" resists; however, achievements of 2 *nm* isolated features and 5 *nm* half-pitch have been reported using inorganic hydrogen silsesquioxane resists [Duan *et al.*, 2010; Manfrinato *et al.*, 2013].

Nano-Imprint Lithography (NIL) - developed by Chou, Krauss, and Renstrom (1996) - is a convenient mechanical method of fabricating low-cost, high-throughput, and high-resolution 3D nanostructures by creating a deformation onto an imprint monomer or polymer resist using a mold, which can then be cured using heat or light to produce nanoscale features. Both scanning beam and probe techniques (like t-SPL discussed below) utilize NIL to attain rapid industry-scale throughputs while retaining great feature resolution. Today, this technique is most notably valuable in producing ultra-high resolution metamaterials.

Other than its slow writing time, one of the primary concerns associated with EBL is the invasive and even destructive nature of higher-dose beams as they can edit the topography of underlying, large screening-length 2D materials, create vacancies, and generate defects. Nonetheless, some have used these "bugs" as features to locally dope semiconductors.

1.1.2 Ionic

This technology is a fascinating consequence of the space race, as it was never intended for lithography but rather for a lightweight alternative to the chemical propulsion of spacecrafts.

Ion-Beam Lithography (IBL) is a versatile variation of EBL using a a beam of charged particles that can be accelerated to considerable energies (traditionally from 20 to 100 keV) focused to a tight beam spot (usually between 1 to 10 nm). IBL can be categorized into three techniques: Focused Ion Beam (FIB), Proton-Beam Writing, and Ion Projection Lithography. FIB instruments - the most popular and developed of the three - utilize particles like helium ($\sim$0.5 nm features), neon ($\sim$1 nm features), and gallium ($\sim$2 nm features) to image, etch, or pattern a wide range of samples [Höflich *et al.*, 2023].

As beamed ions have a much larger momentum than electrons, inelastic interactions with the sample result in less scattering effects making this tool a solid candidate for high aspect ratio 3D nanostructures. Additionally, the increased depth-of-field allows FIB to pattern onto curved and in-homogeneous samples, which can be convenient for condensed matter applications. However, usage of FIB in the fabrication of electronic devices remains difficult as it is an inherently invasive process that causes atomic-scale sputtering, and implanted ions considerably modify semiconductor properties [Hirayama and Okamoto, 1985]. This process was originally too slow for any industrial-scale applications, but advances in gas-assisted etching and more resist-oriented progresses have accelerated fabrication times by orders of magnitude.

1.1.3 Photonic

Lasers and other optical instruments in the far field are practically limited in resolution by **aberrations** in the system and fundamentally by the **diffraction** limit - ultimately setting a fundamental boundary condition on the fabrication and imaging of nanostructures with sizes smaller than that of the utilized wavelength of light. Monochromatic (astigmatisms, defocus, distortions, etc.) and chromatic (axial or lateral) aberrations must be engineered out of an optical system to approach its theoretical resolution limit. A point source of light will be subject to blurriness, since the wave-like nature of light yields diffraction. In the case of a circular aperture as in most laser systems, it is considered to be a two-dimensional analog of the single-slit experiment. This light interferes with itself producing an *Airy* disc-shaped point spread

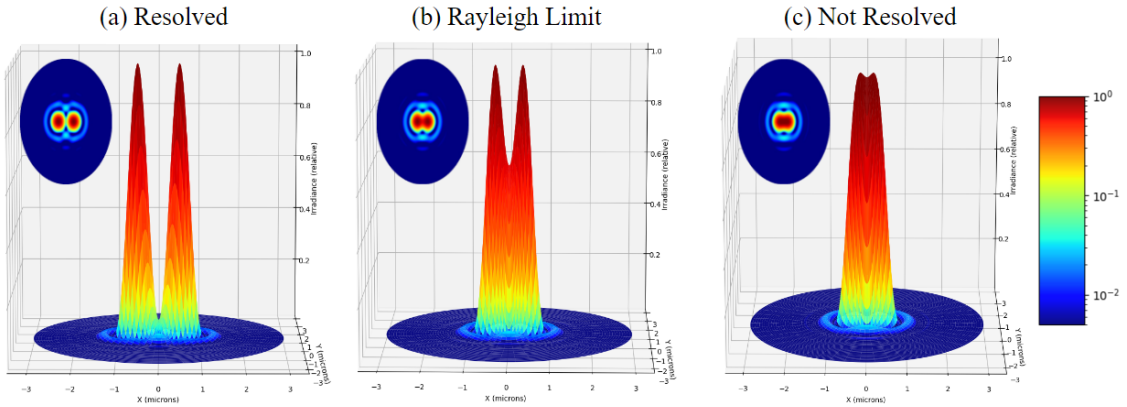

Figure 1.1. Point spread function and 2D top-view simulations of two Airy disk irradiance distributions (normalized) interfering at varying displacements. (a) The features can be resolved. (b) The features are at the Rayleigh limit. (c) The features are within the theoretical limit and can not be resolved. Refer to Appendix A.1 for method.

function (PSF), as illustrated in Figure 1.1. The resolution of a system is generally defined as the smallest distance r between two distinguishable features. Many different standards are discussed in the literature such as the Abbe and Sparrow limits, but we maintain the **Rayleigh criterion** [Meilan and Garavaglia, 1997].

In the ideal case of a Gaussian beam in the far-field, the smallest lateral resolution - or printable "half pitch" - of the spot is determined by Equation (1.1) where λ is the wavelength of the incident light source, n is the index of refraction, θ is the half-angle of the beam source entering the objective, NA is the numerical aperture, and ($k_1 < 1$) is the arbitrarily defined "k_1-**factor**". This last factor can be considered a collection of all other lithographic factors. One way of improving k_1, for example, would be to engage in double-patterning and stitching, which could double the number of steps in the lithographic process, driving up the costs significantly.

$$\Delta r = 1.22\frac{\lambda}{2n\sin\theta} = 0.61\frac{\lambda}{NA} \approx k_1\frac{\lambda}{NA} \tag{1.1}$$

The NanoFrazor's UV laser direct-write system is based on a laser of wavelength 405 nm and a 20x microscope objective with a numerical aperture of 0.4. Given a k_1 of 0.6, this system achieves an optical resolution of 600 nm. Production-grade optical lithography systems cost hundreds of millions of dollars. Advanced Semiconductor Materials Lithography (ASML)

Holding's state-of-the-art extreme ultraviolet (EUV) photolithography machines with meter-long and picometer-rough mirrors achieve an NA of 0.55 while sourcing light at a wavelength of 13.5 *nm* to fabricate nanoscale chip nodes [Ronse, 2024]. Only recently, consumer-oriented producers like Samsung, International Business Machines Corporation (IBM), Taiwan Semiconductor Manufacturing Company (TSMC), and Intel have begun producing chips with a "2-nm" photolithographic process [Kim and Rho, 2024]. However, smaller nodes require substantially more power - in the kilowatt range - causing massive difficulties in optical systems due to high heat generation. As λ and NA seem to reach an economic point of diminishing returns, substantial efforts are being made to reduce the k_1-factor. This can be achieved through clever "process improvements" manifested through novel approaches like "computational lithography" to search for geometric or component-oriented factors during simulations [J. F. Chen *et al.*, 2008].

The high maintenance cost, power requirements, and complexity of these instruments leave much to be desired, so efforts push towards "low-cost" scanning probe alternatives or complements.

1.2 Scanning Probe Techniques

Sharp tips have been employed in a multitude of ways to both characterize and manipulate surfaces at the atomic level ever since the topografiner in 1972 [Young, Ward, and Scire, 1972], the **scanning tunneling microscope** (STM) in 1981 [Binning *et al.*, 1982], and the **atomic force microscope** (AFM) in 1985 [Binnig, Quate, and Gerber, 1986]. An ocean of emerging **scanning probe microscopy** (SPM) techniques ensued. In the sections below, we discuss SPM techniques used to modify (i.e. pattern) surfaces.

1.2.1 Electrical

Atomically resolved manipulation with scanning probes was achieved by Eigler and Schweizer (1990) where they demonstrated the local manipulation of individual Xe atoms on a Ni(110) surface using a $4°K$ ultra-high vacuum STM setup. This led to iconic images and results such as the famous quantum corral by Crommie, Lutz, and Eigler (1993) where 48 Fe adatoms are positioned in a circular ring of radius 71.3 Å on a Cu(111) surface by manipulating the tunneling tip to laterally "drag" the atom to the desired location using repulsive forces. This technique has been subsequently used to build many model systems like magnetic nanostructures and artificial molecules, atom by atom [W. Chen *et al.*, 1999; Yamachika *et al.*, 2004].

One of the most efficient and developed atomically-precise manufacturing techniques has been **Hydrogen Depassivation Lithography** (HDL), which utilizes a bias at the STM tip in order to break the bond between hydrogen atoms and an Si(001) surface, ultimately fabricating the smallest features possible [Lyding *et al.*, 1994]. Many applications such as single-electron transistors [Fuechsle *et al.*, 2012; Rashidi, Vine, *et al.*, 2018], editable atomic-scale memories [Achal *et al.*, 2018], and quantum computer qubits [Bussmann *et al.*, 2021] have been facilitated by HDL. As these require H-saturated surfaces, alternative resists like native oxides, molecules, and halogen atoms [Dwyer, Dreyer, and Butera, 2019; Pavlova *et al.*, 2020] have been recently demonstrated.

Great research efforts were also directed towards using non-contact and amplitude modulation-mode AFM (AM-AFM) for single-atom lateral manipulation on insulating surfaces, which could not be done via STM; impressively, some of the AFM-based techniques can also be performed at room-temperature, avoiding the need for complex cryogenic apparatuses [Oyabu *et al.*, 2005; Sugimoto *et al.*, 2007; Kawai *et al.*, 2014]. AFM proves to be a powerful tool not only for monitoring and manipulating individual atoms at room-temperature but also directly measuring the forces required to position these atoms (in the range of picoNewtons to nanoNewtons) [Ternes *et al.*, 2008]. These SPL techniques display excellent capabilities in locally editing the chemical, mechanical, and electronic properties of samples, allowing for the fabrication of atomic-scale

workpieces.

Electrical currents in STM and AFM setups have also been employed to directly pattern calixarene resists [Kaestner and Rangelow, 2012] and initiate rapid tip-controlled dielectric breakdown to fabricate pores at the nanometer-radius scale [Y. Zhang *et al.*, 2019], enabling applications in nanofluidics and biological sensing.

Oxidation-Scanning Probe Lithography (O-SPL), using a phenomenon known as Local Anodic Oxidation, was developed by Dagata *et al.* (1990) at the National Institute of Standards and Technology. In O-SPL, a water meniscus bridges between the SPM probe and reactive sample; wherein, an electrically controlled oxidation process occurs to pattern the surface. The resolution of this technique is limited by the bridge size rather than the tip radius, which can be enlarged or shrunk by enhancing or decreasing the voltage pulse strength (20 - 30 V) and duration (10 μs - 10 s) [Garcia, R. V. Martinez, and J. Martinez, 2006]. Sub-20nm structures have been observed in single-crystal silicon field-effect transistor (FET) devices [R. V. Martínez, J. Martínez, and Garcia, 2010]. O-SPL can now operate in AFM setups (both in contact and non-contact modes) under room temperature and atmospheric pressure, making it an appealing candidate for academic research.

The merits of electrical SPL techniques may be substantial, but so are the drawbacks. For instance, imaging and characterizing these atomically-resolved devices can be tricky and potentially destructive. There are many approaches to facilitate the process of locating a sample in SPM such as the use and combination of machine-learning SPM libraries (like DeepSPM), microfabricated positioning markers, optical navigation, and capacitive sensors [Krull *et al.*, 2020; Bustamante *et al.*, 2024]. At the atomic scale, minor flaws can pose major issues, so research has also undergone to develop automated tools like convolutional neural networks to identify and characterize single defects before fabrication [Rashidi, Croshaw, *et al.*, 2020]. Intrinsic instrumental issues such as thermal drift and hysteresis lag as well as the complexity associated with ultra-high vacuum environments, specially-engineered tips, and temperature-sensitive environments can lead to a wide range of difficulties in some SPL techniques. High-resolution electrical SPL is also currently too slow to compete with scanning beam techniques,

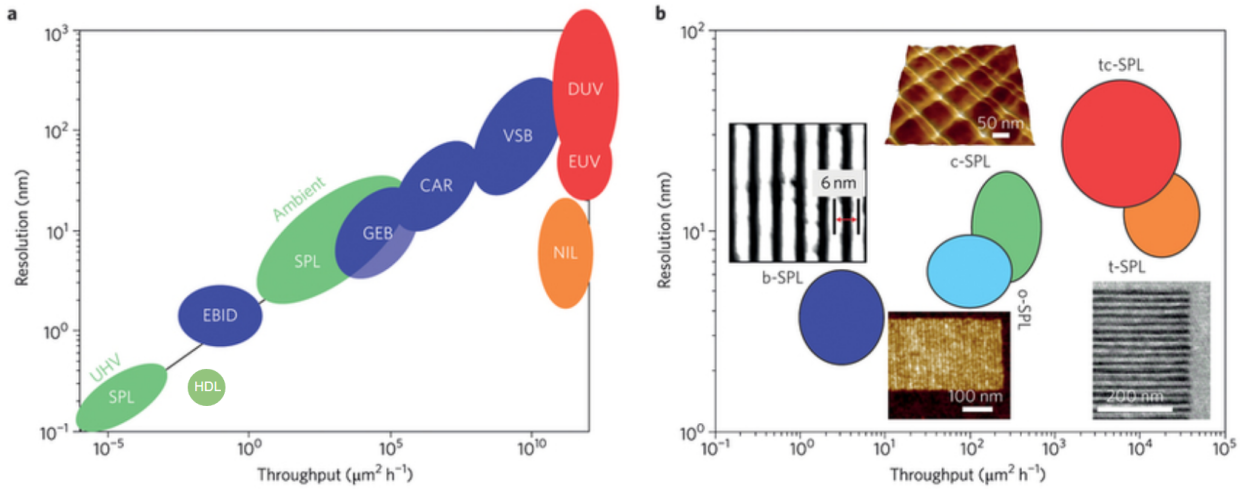

Figure 1.2. Tennant (1999) derives a simplified trend of the lithographic resolution versus areal throughput (μm^2 / hr) for 50% coverage of a surface. (a) The plot fits Scanning Probe Lithography (SPL), Electron-Beam-Induced Deposition (EBID), Gaussian Beam Lithography (GEB), Chemically Amplified Resists (CAR), Variable-Shaped Beam (VSB), Deep Ultra-Violet (DUV), EUV, and Nanoimprint Lithography (NIL). (b) Specific SPL techniques are plotted as well: Bias-Induced SPL (B-SPL), O-SPL, Current-Controlled SPL (C-SPL), Thermo-Chemical SPL (TC-SPL), and Thermal-SPL (T-SPL). Modified from Garcia, Knoll, and Riedo (2014) to include HDL.

as single-tip HDL is noted to achieve a throughput of around 100 surface Si atoms per second at best [Randall *et al.*, 2018]. Observe Tennant's trend in Figure 1.2 for a comparison of throughputs across common nanofabrication techniques.

1.2.2 Magnetic

Shortly after the invention of AFM, Martin and H. K. Wickramasinghe (1987) and Grütter *et al.* (1987) developed **Magnetic Force Microscopy** (MFM) to observe the interaction force between a single-domain magnetic tip and a magnetic sample. Notably, patterning spin textures using MFM can be achieved by approaching the magnetic tip to induce spin reversal of a magnetic nanoparticle on the sample surface; this can be observed in arrays of CoPt with perpendicular magnetic anisotropy [Mironov *et al.*, 2009]. Recent developments report that Kagome artificial spin ices (ASI) and non-interacting nano-magnet arrays can be accessed by writing topological defects into magnetic nano-lines using MFM [Gartside *et al.*, 2017].

1.2.3 Thermal

In the early 1990s, IBM Almaden researchers around Daniel Rugar and John Mamin were concerned with the demand for high-density data storage. After achieving impressive storage densities and writing speeds using the field emission of gold clusters, they began exploring how heated STM and AFM probes could perform data writing and topographic readback on plastic surfaces. Early attempts at write-once and read-only schemes used μs laser pulses to heat a sharp tip and another laser to sense cantilever deflection, which could soften 150-nm indents into polycarbonate [H. J. Mamin and Rugar, 1992]. A closed-loop write-once and read scheme was integrated using a high-frequency, piezoresistive sensor to detect deflection and a separate resistive heater to indent features into soft polymeric materials [H. Mamin *et al.*, 1999]. Although this inspired consumer-oriented device development such as the ambitious Vettiger and Binnig "Millipede Project" in 1995, the competitive scaling of non-volatile and flash memory storage financially outperformed the instrumentally complex AFM-controlled storage. Instead, nanotip lithography techniques proved much more influential in nanoscale fabrication and manipulation for nanofluidics, photonic metamaterials, spin-texture imprinting, and most notably low-dimensional devices. In 2009, researchers at IBM Zurich decided to focus on self-amplified depolymerization polymer polyphthalaldehyde (PPA) and molecular glasses as lithography resists, which would sublime or rapidly decompose into volatile monomers upon tip contact and leave virtually no contaminant residue [Coulembier *et al.*, 2009].

The key selling points of this technique today - in comparison with e-beam, focused ion beam, and optical lithography - remain its sub-resist imaging capabilities, rapid readback, and localized $3 \times 3 \times 3$ nm^3 voxel of heat. The tip-radius-limited lateral feature resolution is competitive with that of state-of-the-art e-beam and optical lithography resolutions [Mojarad *et al.*, 2015]. The ability to image nanoscale features like quantum dots [Huff *et al.*, 2018], wires, and flakes in-situ under considerably thick amounts of resists ($\tilde{2}$00 nm) allows the user to easily design patterns and circuits for fabrication without the need for microfabricated positioning markers. Through this rapid readback, any patterning issues can also be addressed prior to

the development step and in real time, saving considerable resources. Although this technique does not yet provide atomically-resolved fabrication, it does allow for the delicate and precise placement of contacts on monolayers, the fabrication of nanowires, and even the deposition of quantum dots [Ryu and Rodrigo, 2022].

The Nanofrazor Explore system used in this thesis is a commercially available hybrid tool for ultra-high resolution nanofabrication that combines roughly 15-nm-feature closed-loop **Thermal Scanning Probe Lithography** (T-SPL) and 600 nm resolution UV laser lithography. This technique will be explained in greater detail in Chapter 2.

1.2.4 Mechanical

The pressure exerted by a sharp tip onto a sample surface can easily exceed pressures of 1 GPa; this is sufficient to surpass the yield strength of many soft resists, allowing for permanent deformities or nanoscale indentations. Mechanical Scanning Probe Lithography (M-SPL) ploughs, mills, and cuts materials using AFM probes in the contact mode (10^{-8} - 10^{-11} N) at relatively high scanning speeds (roughly 100 μm per second) [Schumacher *et al.*, 1999]. This technique can be used in a a wide range of applications ranging from nanoindented 2D semiconductor Single-Photon Emitters (SPE) [Rosenberger *et al.*, 2019] to nanoindenting protein shells for the study of the mechanical properties of viruses [Roos, 2018]. Various approaches of M-SPL exist, allowing for nanoscale engraving, shaving, scratching, squeegeeing, enrolling of 2D sheets into ribbons, as well as fabrication of complex 3D nanostructures. The high pressure and scan-speed leads to significant tip wear and often requires harder tips to maintain sensible operational lifetimes. The most common option is to use diamond-coated tips. Unsurprisingly, the resolution of M-SPL is limited by the tip radius.

1.2.5 Fluidic

Dip-pen Scanning Probe Lithography (D-SPL) was developed by Jaschke and Butt (1995) and coined by Piner *et al.* (1999). The working principle dictates that a functionalized “ink”-

coated AFM probe interacts with a sample surface through electrostatic or electrochemical reactions in a meniscus-manner reminiscent of O-SPL. **Nanopipettes** and D-SPL probes are compatible with a multitude of "inks" such as polymers, proteins, DNA, inorganic nanoparticles, organic molecules, and metallic ions with spot resolutions between 30 to 100 nm [Wu *et al.*, 2010; Zhou *et al.*, 2013]. Similarly to ink from a macroscopic pen, material carried in the microscopic ink can be deposited on a surface and fixed as the transporting solution evaporates. One evident drawback of this technique directly follows the conservation of mass: as some ink adheres to the surface, less remains on the tip resulting in the potential for inhomogeneous patterning as time goes on.

In Chapter 2, we will first explore the operation and fundamental principles of the thermal scanning probe lithography Nanofrazor tool. We then delve into the bilayer liftoff method of fabrication. In Chapter 3, we discuss prominent methods of sample fabrication as well as the tools and methods used to characterize 2D samples including optical contrast, Raman spectroscopy, amplitude-modulated atomic force microscopy, and depth sensing via thermal scanning probe lithography instruments. This then leads to a general discussion of electrical characterization methods and device architectures specifically tailored for 2D semiconductor samples.

2 Thermal Scanning Probe Lithography

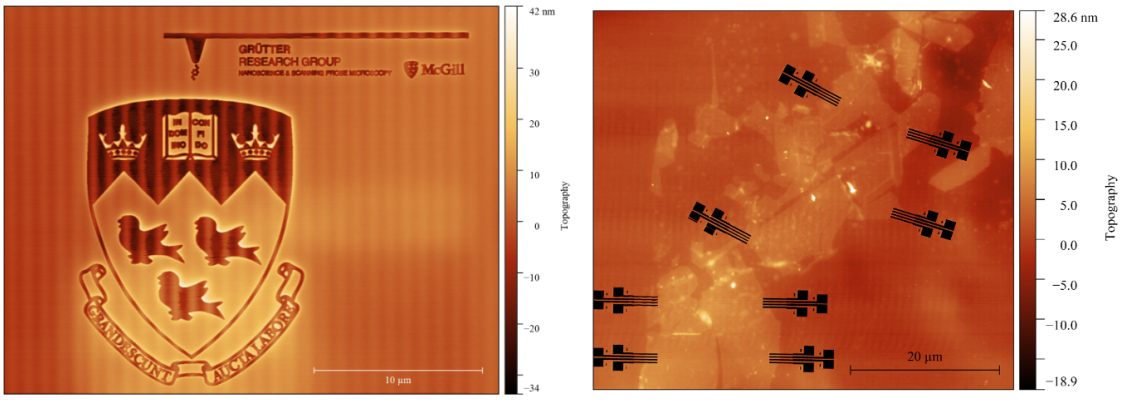

Figure 2.1. T-SPL topographic scans of the nanoscale McGill University and Grutter Group logos on the left and 32 electrical probes patterned at the edges of a large 2D WS_2 flake on the right. These are scans of features patterned in continuous heating-mode into roughly 30 nm PPA / 50 nm PMGI. The fabricated features on the left can be observed in Figure 2.5.

2.1 Working Principle

Thermal scanning probe lithography (t-SPL) demonstrates incredible capabilities for near-atomic scale manipulation of materials. A wide range of nanoscale maneuvers can be performed such as removal (indentation and sublimation), conversion (physical and chemical), and addition (melt transfer and gas phase) of material. In this work, t-SPL is primarily used to pattern electrical probes on 2D semiconductors but has also proven itself to be an excellent tool to conduct in-situ imaging of flakes and fabricate optically visible positioning markers or arbitrary geometries as seen in Figure 2.1.

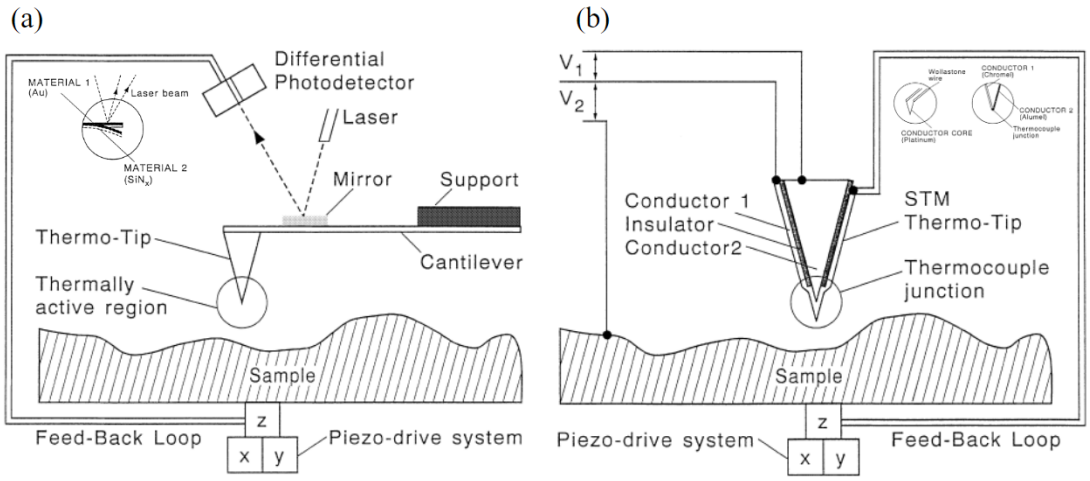

Figure 2.2. Schematics of SThM working principle in AFM and STM-inspired methods respectively. (a) The deflection of the cantilever and bimetallic SiN_X sensor tip ensemble is detected by photodetector differences. (b) The thermo-tip (thermocouple junction) scans the temperature profile of the sample. Modified from Gmelin, Fischer, and Stitzinger, 1998.

2.1.1 Original T-SPL Schemes

Scanning thermal microscopy (SThM) directly senses nanoscale thermal phenomena on sample surfaces. There are multiple working principles and modes, but classically a thermally active probe is positioned at the end of an AFM cantilever for the detection of heat and, more importantly, heat gradients. Prior to the NanoFrazor technology discussed in 2.1.2, original schemes could be categorized into two modes - very much like the ones engineered by Mamin and Rugar - utilizing a photodetector-mirror-laser setup or a piezoelectric cantilever for the detection of nanoscale deflections, sensing thermally-induced tip-sample interaction forces. In these two scenarios, the XYZ directions are controlled by a piezoelectric drive system (similar to most SPM setups).

In the STM-inspired thermal microscopy approach seen in Figure 2.2b, the ultrasharp thermo-tip allows for the extreme spatial resolution needed for near-atomic temperature mapping. A classical STM regulates and measures tip-sample separation by having a servo-loop between a metallic tip and piezo-drive to maintain a constant tip-sample electron tunnelling current. In analogy, SThM uses a thermocouple tip to generate a temperature-dependent voltage V_1 for sensing local tip temperatures; the feedback loop here may then vary the tip-sample separa-

tion during scans to maintain a constant thermocouple voltage between the sample and tip [C. Williams and H. Wickramasinghe, 1986; Dransfeld and J. Xu, 1988]. This alone only provides a topological map of the surface. To simultaneously obtain both topology and temperature mapping, a small temperature variation from heating an electrically conductive sample surface is required; while the probe is vertically vibrated at some feed-back-loop frequency ω_1, the sample temperature is modulated at ω_2 far outside the bandwidth of ω_1 [C. C. Williams and H K. Wickramasinghe, 1988].

The AFM-inspired laser-detector approach in Figure 2.2a uses a sharp thermocouple junction "device" rather than a metallic tip to completely separate the temperature measurement and height feedback sensing, which allows thermal imaging of both insulating and conducting surfaces. As in traditional AFM, laser-detector force-sensing coupled with a feedback loop actuated by a piezoelectric scanner maintains constant force to provide a topographic map. Such devices, using micromechanical sensors, can be used to sense the heat evolution in chemical reactions with deflections corresponding to atto-Joule resolutions. A wide range of different on-tip devices have been reported throughout the years, each with varying applications and goals in calorimetry, biochemistry, integrated circuit analysis, and semiconductor physics [M.-H. Li and Y. Gianchandani, 2003; Lai *et al.*, 1995; Lee and Y. B. Gianchandani, 2004].

2.1.2 NanoFrazor Operation and Read-Write Implementation

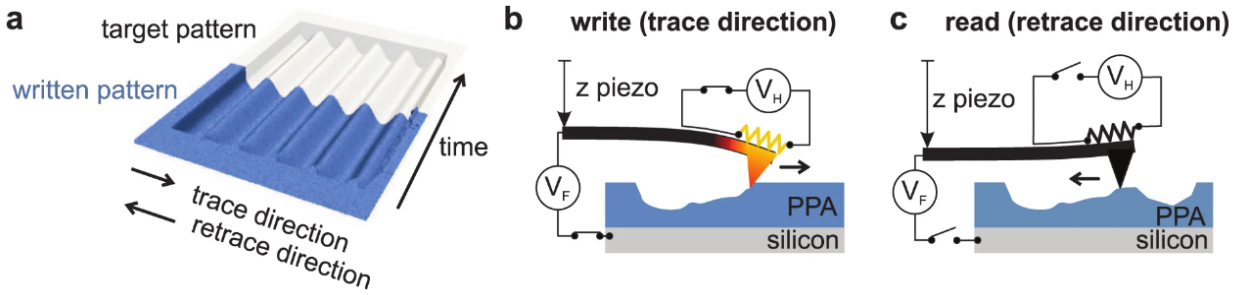

Figure 2.3. Schematic of the trace and retrace capabilities in t-SPL instruments. In (b) we can observe an attractive loading force being activated to sublime the PPA using the highly resistive tip. In (c) we can observe the retrace direction for thermometry to scan the heat conductivity of the sample surface. Reprinted from the Nanofrazor Explore system documentation.

Unlike the previously mentioned versions of t-SPL, the NanoFrazor system requires no optical beam deflection and does not sense forces but only gradients in temperature. Specially engineered Nanofrazor Explore t-SPL cantilevers offer both writing and rapid readback features as illustrated in Figure 2.3. A highly localized, $3 \times 3 \times 3$ nm^3 voxel of heat is generated by a current flowing through the highly resistive tip allowing for a wide range of temperatures from room temperature to 1100 $^\circ C$. Low and high resistance patterns on the cantilever and tip are generated by modulating the dopant concentration, thus generating a resistive heater localized at the tip apex connected with low resistance current carrying wires (conductive legs). Note that the tip temperature is monitored through resistance measurements. Increasing the current through the resistive heater allows heat to flow as a function of the separation from the tip to the sample. While scanning in the $\hat{x}$- and $\hat{y}$-directions, the system reads and engages its feedback mechanism to maintain constant tip resistance, allowing for a contour map of constant heat flow across the sample. This map must then be digitally converted to depth and structural information using calibration parameters.

This conversion process heavily relies on Current-Voltage, Temperature-Voltage, and Reader Signal versus Tip Height Above Surface calibration curves as seen shown in Figure 2.4. IV and TV curves provides information regarding the tip-resistance, operational current during reading and writing, quality of the highly resistive tip, and its threshold temperatures. Analogous to force-distance curves in AFM, the signal-height curve uses a piezo approach and retract of the tip-sample system to calculate the adhesion length, an estimate for the tip height, and the sensitivity. The variable most responsible for read-write quality is the adhesion length, with an excellent threshold traditionally under 20 nm. The adhesion length is measured as the displacement between the "snap-in" point of the approach and the "pull-off" point of the retract. Most lithography in this thesis was performed at an adhesion length in the range of 4-15 nm. The tips were changed out when the adhesion length exceeded 50 nm, roughly after 20 hours of active usage. In AFM force-distance curves, the area between the approach and retract is considered the adhesion energy. Interestingly, in t-SPL, this quantity holds units of volt-meters, producing a concept of adhesion flux. The voltage at the adhesion length provides

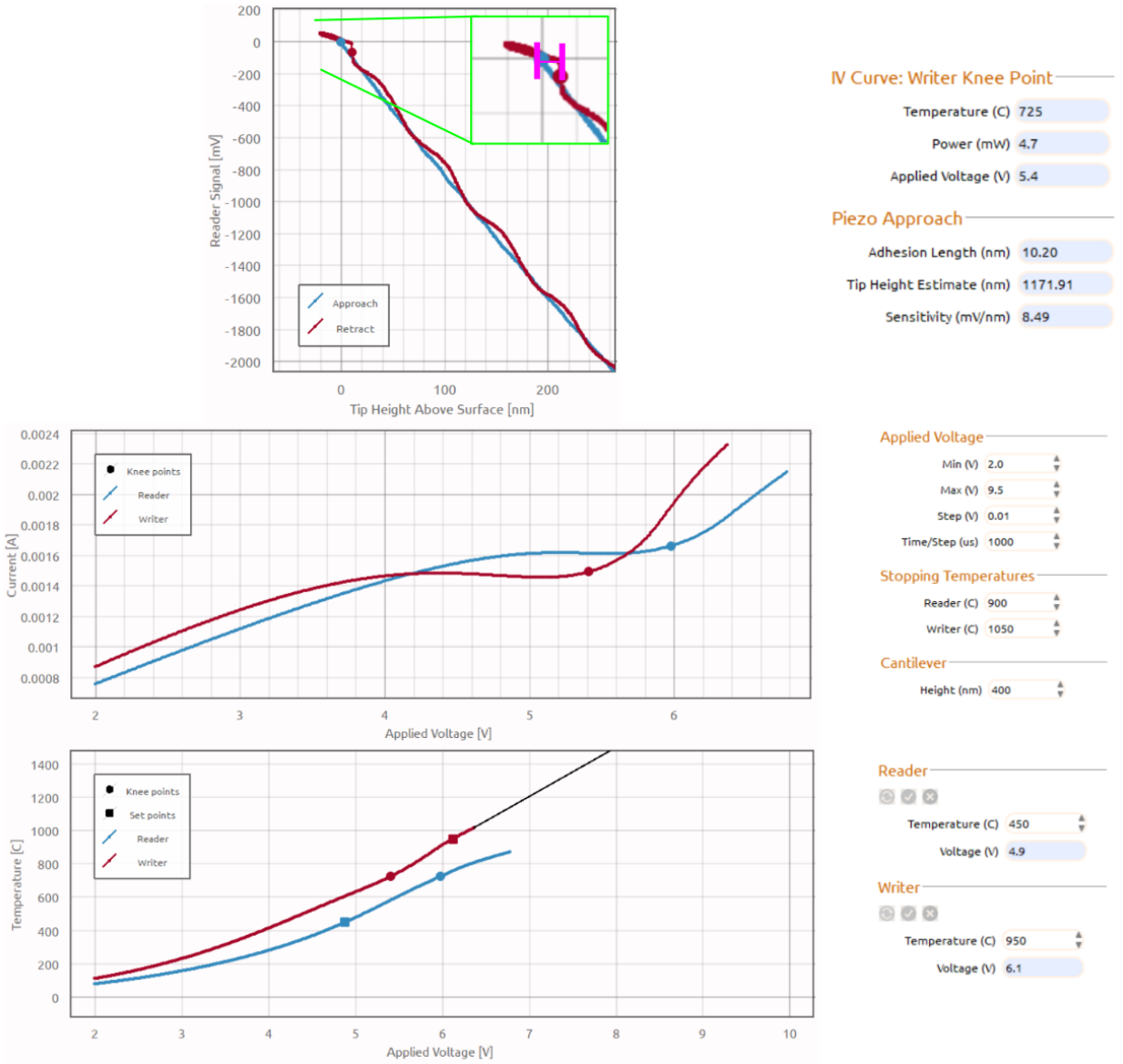

Figure 2.4. Calibration plots and parameters for Reader Signal-Tip Height Above Surface (top), Current-Applied Voltage (middle), Temperature-Applied Voltage (bottom). The Reader-Writer calibration was conducted at a tip-sample separation of 400 nm. The adhesion length measured in this example is 10.20 nm, confirming the quality of tip. Measurements above 50-80nm prompt a cantilever change.

the loading force discussed below.

For programmable patterning capabilities, the sample is translated using the stage controller; a bias voltage is applied between the substrate and cantilever to engage an attractive loading force that pulls the cantilever towards the polymer at each individual pixel. This loading force can then be adjusted through capacitive force interactions between the sample and

tip. Writing may either be performed via continuous heating of the tip (direct-current) or by pulsing microsecond increments (alternating-current) of heat onto the resistive tip. Selection of a heating method will strongly depend on the experiment or application at hand with 3D nanostructure applications as seen in Figure 2.7(b) benefiting most from the AC mode for spatial and temporal localization of the heat; DC writing instead results in very little depth of field, more applicable for mono-depth patterns like the ones in Figure 2.7(a).

Imaging and writing speeds using a single tip (as in this thesis) at 50 nm pixel resolution can reach 1000 $\mu m^2/min$ and 10 times that using a parallel decapede tip arrangement. The ideal stage accuracy during field stitching and overlaying of programmed patterns is 25 nm.

2.1.3 Optical Writing

A diffraction-limited, UV-laser writing tool operating at a wavelength of 405 nm and 300 mW power is also integrated in the Nanofrazor Explore instrument producing large-scale patterns as seen in Figure 2.5(b). It similarly also sublimes PPA by heating the laser spot region beyond the gaseous phase transition point. The tool utilizes the thermal probe to guide its lateral movement and focus its beam using relevant height information. During this thesis, the 100,000 $\mu m^2/min$ throughput of the optical instrument has been extremely useful in patterning large-scale electrical circuits, bonding pads, and indices like arrows and texts.

2.2 Bilayer Lift-Off

The bilayer lift-off (BLO) method is generally considered the simplest process to transfer additive structures to a surface, well suited for the non-invasive deposition of metals onto sensitive materials like 2DMs and nanowires. This process relies on an isotropic (wet-etch) development; the bilayer design, as opposed to the fundamental t-SPL tip resolution, limits the size and shape of the evaporated features. Metallic features with a lower-bound resolution of 40-100 nm were consistently achieved using the BLO process described below. Smaller features

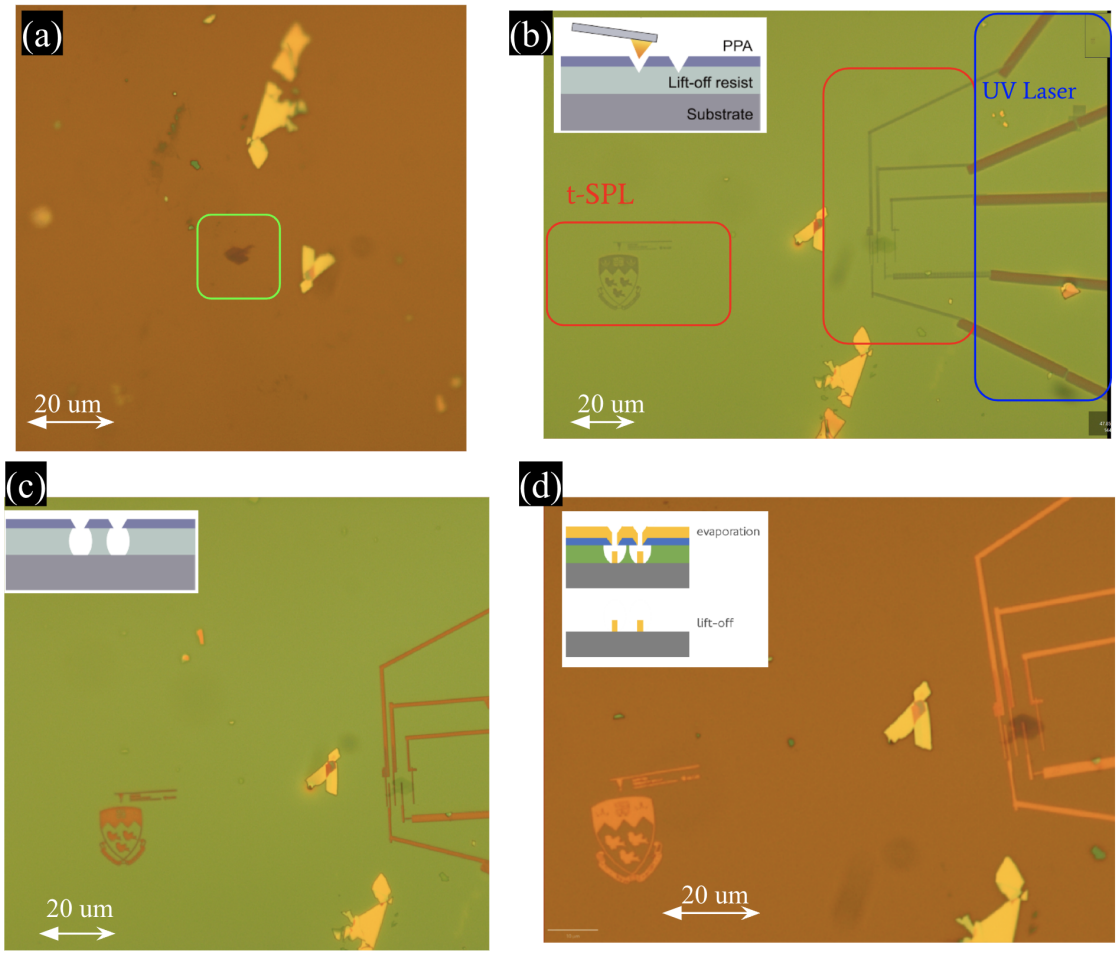

Figure 2.5. Micrographs and relevant inset illustrations of the bilayer liftoff steps covering (a) the optical identification of the flake before spincoating the polymer resists, (b) patterning onto the PPA resist using both the heated probe and UV laser lithography methods, (c) development of the underlayer PMGI, (d) metal evaporation and liftoff of the complete multi-layer (Au/Ti/PPA/PMGI) stack.

like sub-10-nm gaps are feasible using the Nanofrazor in a more complex high-resolution lift-off (HRLO) process with a silicon hard mask transfer layer [Wolf *et al.*, 2014; Ryu Cho *et al.*, 2017]. Take a look at Figure 2.5 for an overview of the complete bilayer liftoff process along with appropriate inset illustrations. In (a), we identify and classify the flake using the optical contrast and AM-AFM methods discussed in the introduction. Subsequently, layers of PMGI and PPA are individually spin coated and baked to harden before t-SPL patterning can occur as seen in (b). The chip is submerged in a development, or wet-etch, solution for a given amount of time to dissolve the exposed underlayer as seen in (c). The chip can then be placed in a metal evaporator to deposit thin layers of adhesive (Ti) and conductive (Au) metals. Finally,

the stacks can be “washed away” using a remover solution in the lift-off process revealing the nanofabricated patterns as seen in (d).

2.2.1 Spin-Coatable Resist Selection

After experimenting with Lift-Off Resists (LOR) 3A and 5A as well as PMMA/MA (AR-P 617, Allresist), it was found that a combination of PMGI and PPA produced cleaner, more consistent, and higher-resolution results for the reasons discussed below.

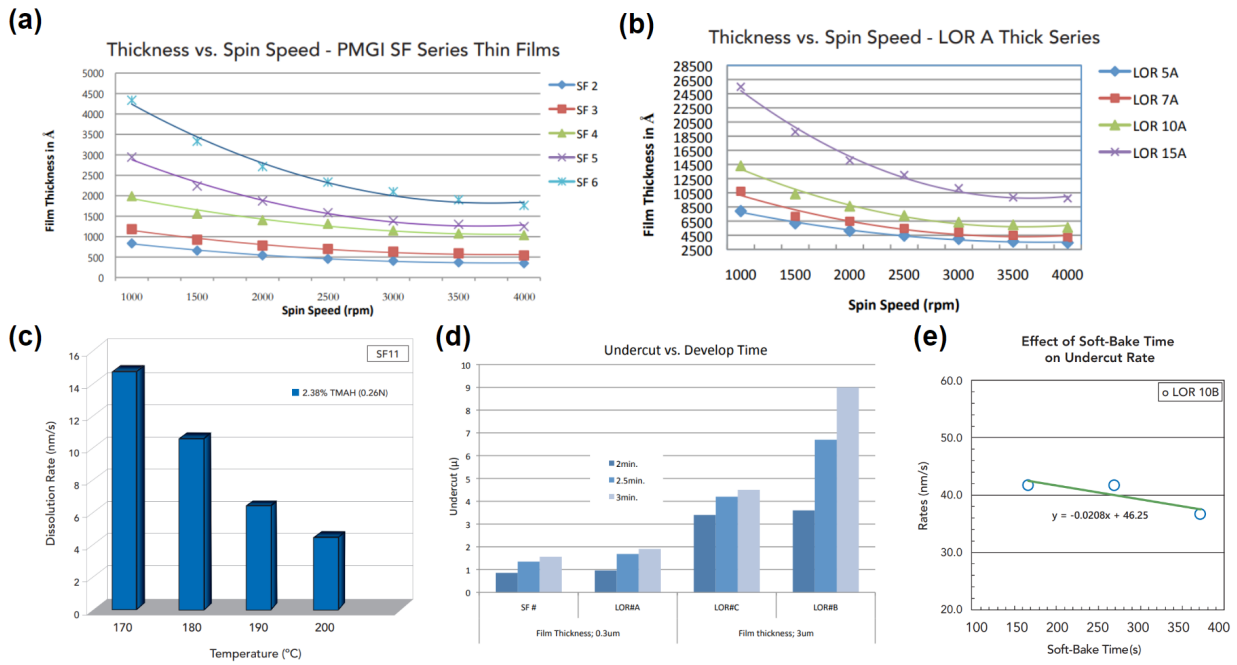

Figure 2.6. Modified from Kayaku (2002). Observe in (a) and (b) the thickness curves of PMGI SF and LOR Series A resists as functions of spin coating speed. From (c) we can estimate the effect of PMGI SF soft-baking temperature on the dissolution rate during wet-etching in a tetramethylammonium hydroxide-based solution. In (d), we can predict the undercut size with respect to development time. The plot in (e) provides a correlation between the undercut rate and soft-bake time, reducing the risk of under- or over-development during trials. This technical data sheet was instrumental in making educated guesses in preliminary trials. Parameters were fine tuned according to the discussed results.

Polydimethylglutarimide (PMGI)

PMGI has a considerably low surface energy allowing it to stick well to hydrophobic surfaces

such as a silicon substrate. Our samples were on a SiO_2/Si substrate, which is hydrophilic. Hexamethyldisilazane (HMDS) pre-treatment makes the substrate hydrophobic, as it leaves methyl groups behind to bond with OH molecules and develop stronger adhesion. Although the NanoFrazor technical documentation strongly recommends this adhesion promotion, the industrial provider of PMGI indicates this step is typically not required [Kayaku, 2002]. Either way, we did not use HMDS, as it is a highly toxic and volatile chemical that must be handled in specialized vacuum chambers. For this reason, it was critical to remove any humidity and effectively clean the substrate with a standard procedure using ultrasonicated acetone, de-ionized water, and 2-Propanol in that order before baking it at 200°C for 3-5 minutes. The ultrasonication of the substrate in acetone must be done carefully as not to disturb 2D samples. If this is a concern, carefully drain acetone onto the sample with a pipette. PMGI SF-2 additionally serves as an excellent under-layer candidate for high-resolution processes due to its ultra-thin spin curve (in the range of 800 to 500 Å for 1000 to 4000 RPM speeds respectively for 45 sec each) and slow-development speed ($\sim$ 1 nm/s). Recall that the thickness of a spin-coated film follows the relation $t \propto \frac{1}{\omega}$ as in Figure 2.6(a and b) with various coefficients like solvent content, vapour pressure, local clean room temperature, and humidity levels affecting the relation. In this work, the PMGI SF-2 was spin coated at a speed of 2,000 RPM for 45 sec and acceleration/deceleration of 10,000 RPM/sec for 0.2 sec to achieve a film thickness of roughly 55 nm. Film thicknesses were not confirmed via ellipsometry; however, maximum depth profiles of patterns in t-SPL confirmed PPA thicknesses.

Polyphthalaldehyde (PPA)

Positive thermal resists are susceptible to sufficiently high temperatures and are removed from areas exposed to localized heat. At elevated temperatures, known as trigger points, localized heat can either soften the PPA homopolymer above its glass transition point ($\sim$ 150°C) for plastic deformation or nanoindentation or directly sublime the polymer straight from its solid to gaseous phase ($\sim$ 180°C). Its low ceiling temperature of roughly 40 °C explains its ability to

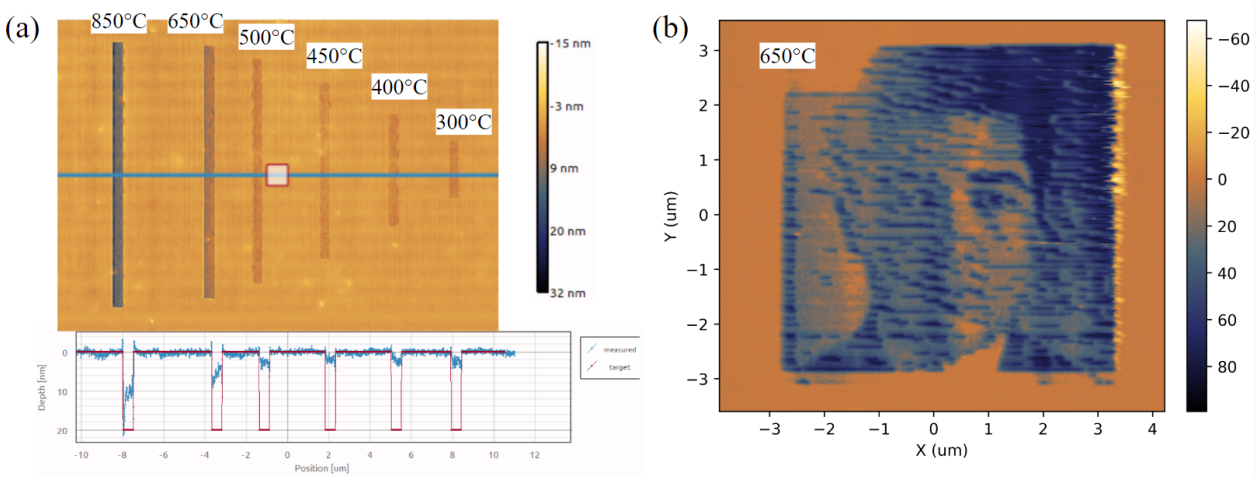

Figure 2.7. Thermal scanning probe topography scans of (a) PPA temperature-depth relations of 1 μm-wide 20nm-deep target patterns on a 8nm-thick PPA and 32nm-thick PMGI stack, (b) PPA for 3D patterning applications (my face on a 6×6 μm^2 canvas). Patterns in (a) were written using continuous (DC) heating mode; while, 3D depth in (b) was written using 25 μs pulsed (AC) heat. Both were scanned and written at a speed of 2 Hz in a read-write feedback loop.

easily decompose into monomers [Aso, Tagami, and Kunitake, 1969]. The ceiling temperature of a polymer generally refers to a point of equilibrium between the polymerization and depolymerization rates; high molecular-weight polymerization ideally no longer occurs beyond this temperature. The ceiling temperature of a polymer is

$$T_C = \frac{\Delta H}{\Delta S + R \cdot log[M]} \tag{2.1}$$

where R is the ideal gas constant, ΔH and ΔS are the enthalpy and and entropy respectively - related by the Gibbs Free Energy $\Delta G = \Delta H - T\Delta S$, and M is the concentration.

Upon this point, with no contact or mechanical force, the polymer chains break and unzips its polymer backbone into volatile molecules through a process known as self-amplified depolymerization. This rapid, endothermic reaction ensures that the produced gas does not accumulate along the surface or more importantly on the tip. Additionally, the rapid localization of the heat on the probe allows for fast patterning of the PPA, which in turn maximizes the throughput of the lithographic technique (1 μs heating pulses). PPA is an ideal tool for the non-invasive patterning of features on underlying samples as it only requires localized heat

to sublime rather than optical, electronic, or ionic sources. As you can see in Figure 2.7, the patterning depth strongly depends on the patterning temperature. This result is expected as patterning efficiency above T_C increases with temperature. Physically, this result is also sound as more generated heat per cubic nanometer can be absorbed by the PPA for sublimation. The ability to control the depth of the localized heating probe allows for extraordinary 3D applications as seen in 2.7(b).

PPA PH75 from Polymer Solutions Inc. was chosen for its longer shelf life, chemical resistance, and higher sensitivity and patterning efficiency than the Phoenix 81 alternative. The PPA comes in the form of a powder that can be constructed using methoxybenzene ($CH_3OC_6H_5$), also known as anisole. The film thickness to be spin coated firstly depends on the weight concentration of PPA powder-to-anisole with the thinnest films at 0.5 (wt%) allowing for 8nm at 6,000 RPM and 11 nm at 2,000 RPM. In this work, based on the designed bilayer for our purpose, we chose to construct 2 (wt%) PPA spin coated at a speed of 6,000 RPM and acceleration of 1305 RPM/sec to produce roughly 35 nm films [PolymerSolutions, 2022]. One must be careful in doing so as coating small, circularly asymmetric samples at high speeds can result in the sample flying off, since the vacuum pressure is insufficiently low in counteracting the centripetal forces on the spin coater.

2.2.2 Baking

Upon spincoating, each polymer resist must be baked; the baking temperature is the parameter with the greatest influence on the polymer's undercut and dissolution rates. For optimal results, the baking time and temperature were chosen to be 200 $^\circ C$ for 200 seconds which resulted in a development rate of 4 nm/sec and an undercut rate of roughly 8 nm/sec in the chosen developer solution. Recommended durations were presented in the Kayaku Advanced Materials LOR and PMGI data sheet [Kayaku, 2002].

It is critical to allow cooling before spincoating the next polymer (PPA) as it may otherwise harden during the spincoating process and result in an undesirable surface. The PPA was then

soft-baked at 85 $^{\circ}C$ for 4 min to produce the best patterning results.

2.2.3 Development and Metal Deposition

After patterning at a target depth of roughly 5 nm more than the PPA thickness to ensure that the PMGI is exposed, the development process may begin. In this work, it was found that a solution of 17 mL AZ 300 MIF (Metal Ion Free) + 0.9 mL H_20 worked nicely to dissolve the underlayer in around 15 sec at a rate of roughly 4nm/s. The undercut development time must be found through trial and error, and roughly 3 additional seconds resulted in a clean lift off process due to a large sufficiently large undercut. To quench or halt the development process, the sample must be rinsed in deionized water for 5 sec, rinsed in 2-Propanol for 5 sec, and then dried with compressed gas. This step is by far the trickiest in the bilayer liftoff as an error of 10 seconds in the development can result in 150 nm of additional or missing undercut as seen in Figure 2.6(d), which can be disastrous in the fabrication of 20nm-tall features. Also, due to the isotropic propagation of the dissolution, a rule-of-thumb is that the patterning resolution is roughly limited by twice the underlayer thickness.

Upon successful wet-etching, thin films of metal may be deposited onto the substrate and semiconductor using an e-beam evaporation technique. In this work, we used a BJD E-Beam Evaporator to deposit 5 nm of Ti as an adhesive layer and usually around 20 nm of Au to ensure electrical transport. The Au thickness was adjusted with respect to the designed PMGI underlay thickness to ensure a clean liftoff process. It is generally recommended that the metal stack is no more than half of the underlayer thickness.

2.2.4 Lift-Off and Potential Misfortunes

To begin the lift-off process, the chip must be completely immersed in DMSO or N-Methyl-2-Pyrrolidone (NMP) remover. The duration and concentration do not matter. Optionally, the remover liquid may be heated to accelerate the lift-off process. For a clean lift-off process, the PMGI thickness must generally be larger than the deposited metal stack by roughly 1.5 times.

As seen in Figure 2.8, this procedure is prone to many potential flaws.

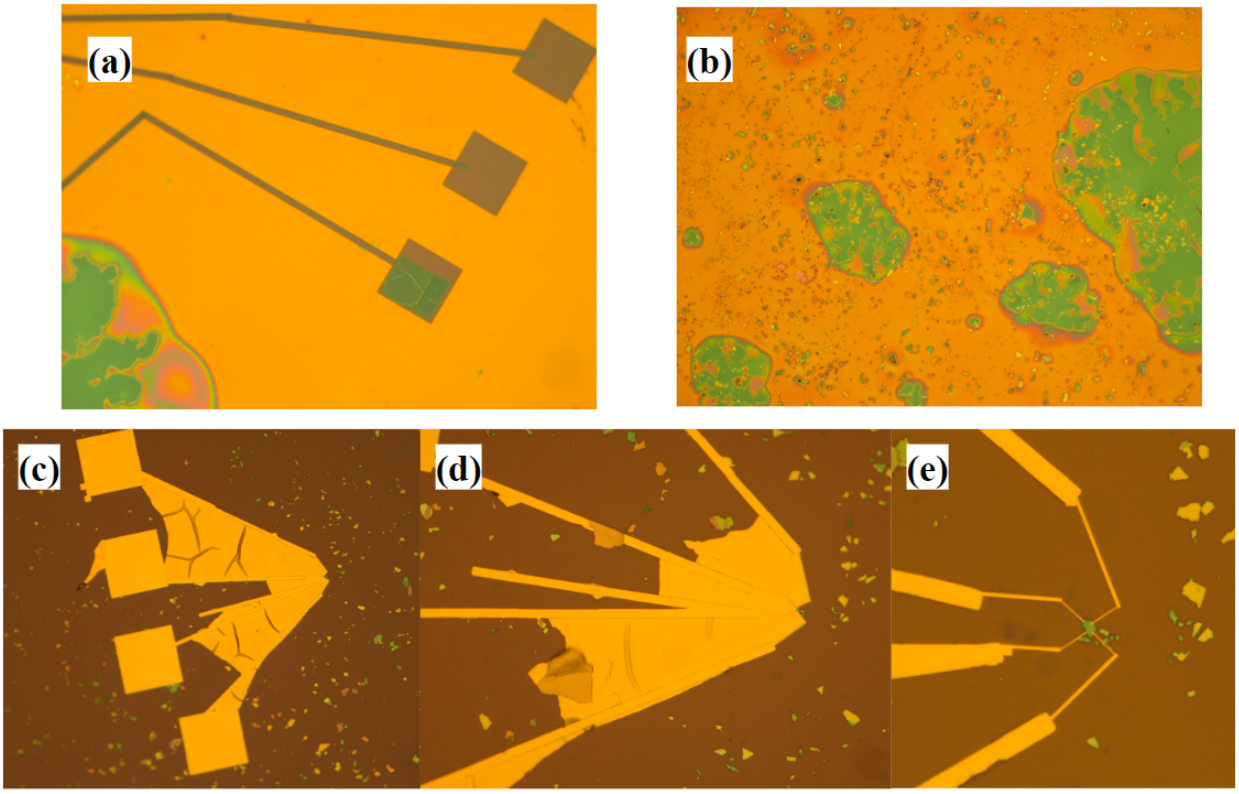

Figure 2.8. Micrographs of a handful of interesting fail cases: (a) Laser lithography sub-dosage, (b) Tall WS_2 causes large capillary forces leading to tearing of the thin PPA overlayer, (c-e) Overdeveloped undercut likely causes PPA overlayer to bend downwards at the edges into the hollowed out cavity; gold from the top layer may then bond to electrodes as illustrated in Appendix A.2.

Below are a few thoughts pertaining these failure scenarios:

1. Case (a) is a direct result of under-dosage during the UV lithography process. Many repairs and adjustments to the laser system were made during the duration of this thesis. As a result, the intensity of the beam was often sub-optimal and extending the dosage durations did not always produce the intended sublimation of the PPA resist. As shown in the image, blue-coloured films of PMGI remain on the patterned bonding pad regions indicating that a thin layer of PPA remained above it, ultimately inhibiting it from being properly dissolved by the developing solution. This is further supported by the folds in the remaining PMGI film. Considerably increasing the dosage (exposure) during UV laser lithography fixed this issue. Conducting dose-response tests and measuring power before

patterning can also help reduce the chance of under-dosing the PPA.

2. Case (b) was a recurring issue at the start; especially when we began using thinner films of (8nm) PPA and (32nm) PMGI on mechanically exfoliated flakes. At first, it was believed that tape residue on the substrates was causing the mysterious nucleation sites. The existence of abundant residue content was not supported by Raman spectroscopy performed on samples. A more plausible explanation was that tall WS_2 flakes on the order of 40+ nm (similar to the resist stack thickness) resulted in large capillary forces, ultimately bursting through the resist during spincoating. This was confirmed by using thicker resists on the same samples. Ultimately, maintaining thin polymer stacks required adjustments in the spin coating accelerations recipes. Those were reduced for PPA from 10,000 to 2,000 RPM/sec to account for capillary forces, which both resolved the issue and allowed for thin resists to be used.

3. The case from (c-e) was a fortunate solution through improvisation. It was noted after lift-off that much of the Au remained between probes, ultimately shorting the device. From the visible folds in the unwanted film, it was hypothesized that the Au "tarp" was not bonded to the substrate. Upon careful sonication in deionized water, this was confirmed. The sample was sonicated for 10 sec and re-inspected for cleansing effects. This was done roughly 8 times. Progress starting at (c) and ending at (e) can be observed in the figure. The underlying reason for this failure is likely over-development of the PMGI underlayer. It is most plausible that the undercut was too deep, causing the PPA above it to structurally fold downwards as illustrated in Appendix A.2. As a result, Au film on the PPA bonded to the Au/Ti inside the patterned region. It is possible that the remover solution heated during the final lift off process at a temperature $> 100°C$ approached the glass transition point of PPA, enabling the fold through non-negligible capillary forces.

By the end, the overall yield of the nanofabrication process had reached roughly 50% with the least successful step being spin coating of the resists. To improve this in the future, using larger (4 ×4 rather than 2×2 cm^2) and more square silicon chips would alleviate a lot of the

surface tension issues at the edges of the chip during spincoating.

2.3 Observed t-SPL Flaws

Outside of some read-write feedback, tip calibration, and cantilever quality issues, two recurrent and major flaws became apparent in the usage of the system:

1. Stage Controller (Piezo) Problems

   (a) There were several occurrences during which spatial translations programmed in the software to move the stage resulted in violent snap-backs. These were later understood to be results of a broken piezo and stage controller that had to be replaced. This affected both t-SPL and laser writing operations.

   (b) A more fundamental issue was stage drift between scans that resulted in shorted contact patterns as seen in Figure 2.9(a). As discussed previously, overlay and stitching resolution tends to be around 25 nm in ideal conditions. This accuracy was observed on many occasions prior to stage controller repairs to rather be on the order of microns.

Random Walk - Tip Squeegeeing

1. The root of this issue is less understood and observed in Figure 2.9(b). Note that the system is vibrationally protected by three layers of acoustic isolation (>98 percent at 10 Hz). This occurred often resulting in surface-level taps, indentations, and nano-cuts into the PPA. Large, random elliptical taps at the edges on the order of 1-10 nm depths and 100-300 nm major axes could be observed around an imaged flake as in Figure 2.9(c). The squeegeeing in (b) and (d) could be observed on many samples different samples between scans; depth never exceeded the thickness of PPA, so the consequences were negligible.

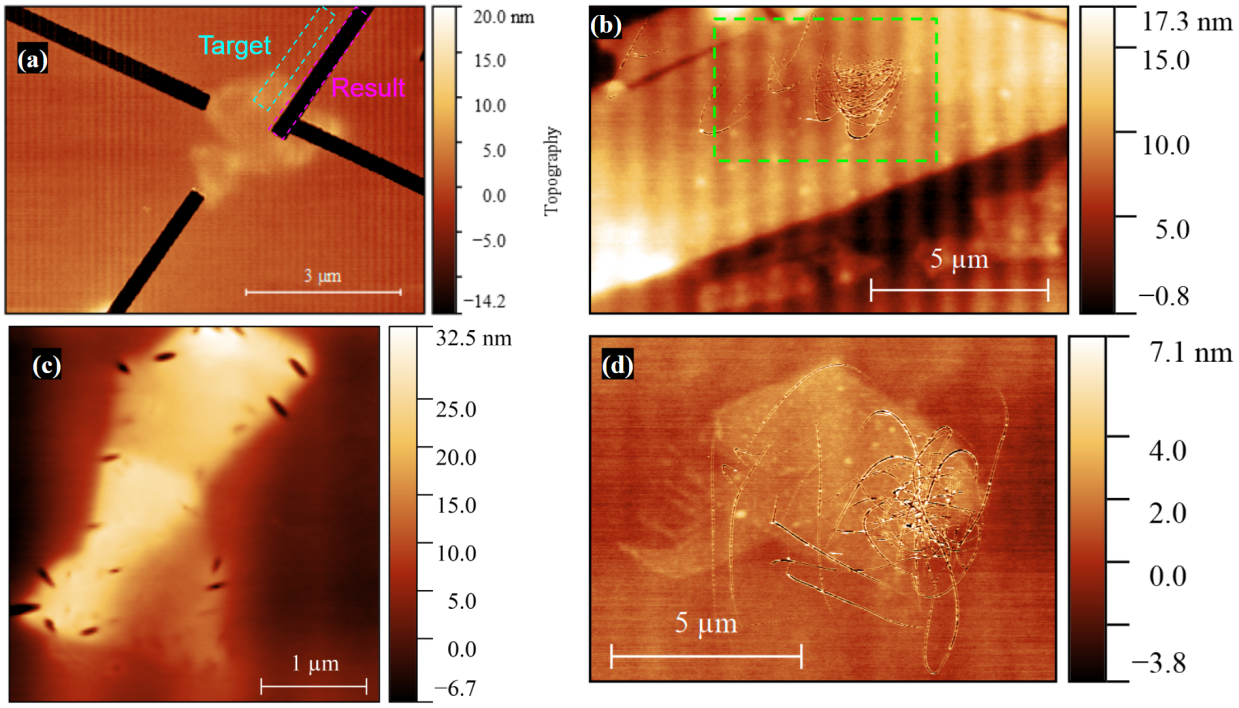

Figure 2.9. Topographic images of: piezo drift overlay issue (a), "random walk" squeegeeing (b and d), and light tapping at the edges of flakes (c). These t-SPL topography scans are of patterned PPA on PMGI/WS_2/SiO_2/Si.

3 Sample Preparation

3.1 Two-Dimensional Materials

In materials science, two-dimensional (2D) van der Waals (vdW) materials refer to crystalline or paracrystalline solids consisting of a thin nanosheet of a material - generally a single atom in thickness. They have an anisotropic electronic and chemical structure with strong covalent bonds along an in-plane axis and weak vdW bonds along the out-of-plane axis. Some popular examples include graphene, hexagonal boron nitride (h-BN), the family of transition metal dichalcogenides (TMDs), phosphorene, perovskites, metal oxides, and polymers. The ability to fine-tune and engineer the size and shape a material's band structure is critical to solid-state electronic and optoelectronic technologies.

Atomically thin 2DMs offer new approaches of tuning the bandgap by altering - for example - chemical composition, background doping or lattice constant through mechanical strain, spatial extent (quantum confinement) and the heterostructuring of other materials, as well as Coulomb engineering through the modification of local dielectric environments [Raja *et al.*, 2017]. It is observed that 2DMs, and more specifically 2D TMDs, can present a wide range of electrical and optical band gap-related characteristics depending on the the material thickness and phase. For example, MoS_2 highlights three phases including 3R, 2H, and 1T/1T'. The 3R and 2H phases exhibit semiconductor properties with high carrier-mobility and the potential for energy storage devices like sodium and lithium batteries as well as flexible transistor and supercapacitor technologies; however, the 1T/1T' phase exhibits metallic properties usable in electrocatalytic hydrogen production due to the its peak conductivity [Ho, Y.-H. Wang, and

H.-Y. Chen, 2014]. Symmetry has played a vital role in the engineering of band structures and consequently crystal properties; consequently, this has made SPMs excellent tools to investigate 2D materials. Ever since the synthesis of atomically-thin semiconductor films using chemical vapour deposition (CVD) and physical vapour deposition (PVD) techniques such as molecular beam epitaxy (MBE) and, more recently, mechanically exfoliated sheets, researchers have endeavoured to manually architect properties into the vertical structure of materials; this is known as rational design [C. Wang *et al.*, 2023].

In the case of TMDs (e.g. WSe_2, $MoSe_2$, WS_2, and MoS_2) following an MX_2 structure, their bulk is spatially inversion-symmetric which is broken when exfoliated down to the monolayer level [Xiao *et al.*, 2012]. This, along with spin-orbit coupling (SOC), allows for a multitude of spin-valley locking-induced phenomena such as Ising superconductivity, valley-polarized excitons, and the valley Hall effect [Saito *et al.*, 2015a; Kin Fai Mak *et al.*, 2012; K. F. Mak *et al.*, 2014; Saito *et al.*, 2015b; Xi *et al.*, 2015]. A plethora of novel physical phenomena like Moiré superlattices, ferromagnetism, ferroelectricity, Wigner crystals, and Weyl semimetals drive the world of 2D physics today. A solid understanding of their surface physics and electrical properties is essential to manipulating their characteristics to build successful devices. Vigilant nanofabrication practices and meaningful material selection of 2D metal-semiconductor junctions is most critical in the endeavour for ohmic contact or low Schottky barriers in 2D devices [Zheng *et al.*, 2019].

3.1.1 Mechanical Exfoliation

Ever since Novoselov, Geim, *et al.* (2004) brought graphene to the public eye, many methods of preparing nanosheets from bulk have been developed such as mechanical exfoliation, liquid-phase ultrasonic exfoliation, and ion intercalation exfoliation; these are common forms of top-down exfoliation methods [Novoselov, Jiang, *et al.*, 2005; Jawaid *et al.*, 2015; El Garah *et al.*, 2018]. Bottom-up methods like CVD can grow 2D TMDs onto a substrate through means of thermal vaporization; while CVD is powerful for the growth of large surface area monolayers,

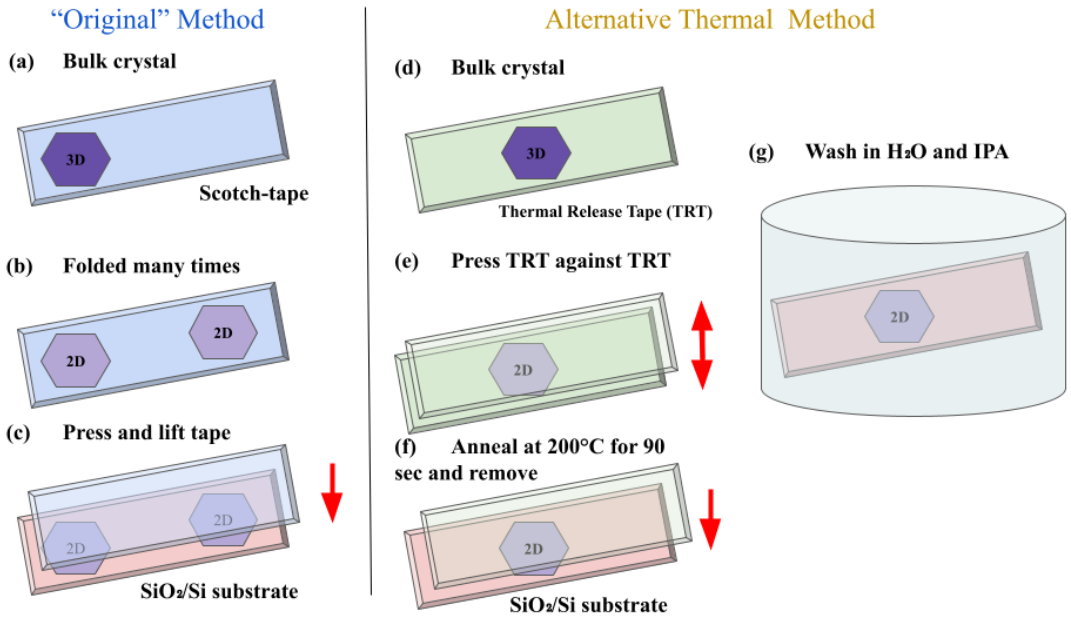

Figure 3.1. Schematic illustration of the steps in both the original and the thermally-assisted mechanical exfoliation methods.

the lower quality resulting from unwanted defects often hinders its application in 2D devices [Zafar *et al.*, 2016]. Mechanical exfoliation - also sometimes called micromechanical cleavage - remains today the most popular, straightforward, and altogether cost-effective method of preparing TMD flakes at an academic scale. Many methods ranging from gel and Au-assisted exfoliation to multi-step processes including thermal activation, etching, and washing have been recently developed to optimize the shape, surface area, residue content, and quality of mechanically exfoliated 2DMs [Y. Li *et al.*, 2022].

In this thesis, we utilize both the "original" process and a variant of the thermally-activated method to prepare WS_2 samples. Take a look at Figure 3.1 for an illustration of the exfoliation processes. These produce a wide variety of 2D flakes ranging from 1 to 20 μm in diameter and 1 to 10+ layers in count.

3.1.2 Layer Count Classification

One difficulty in 2D experiments is the classification of samples by layer count. A combination of optical and AFM height measurements are usually used to count the atomic lay-

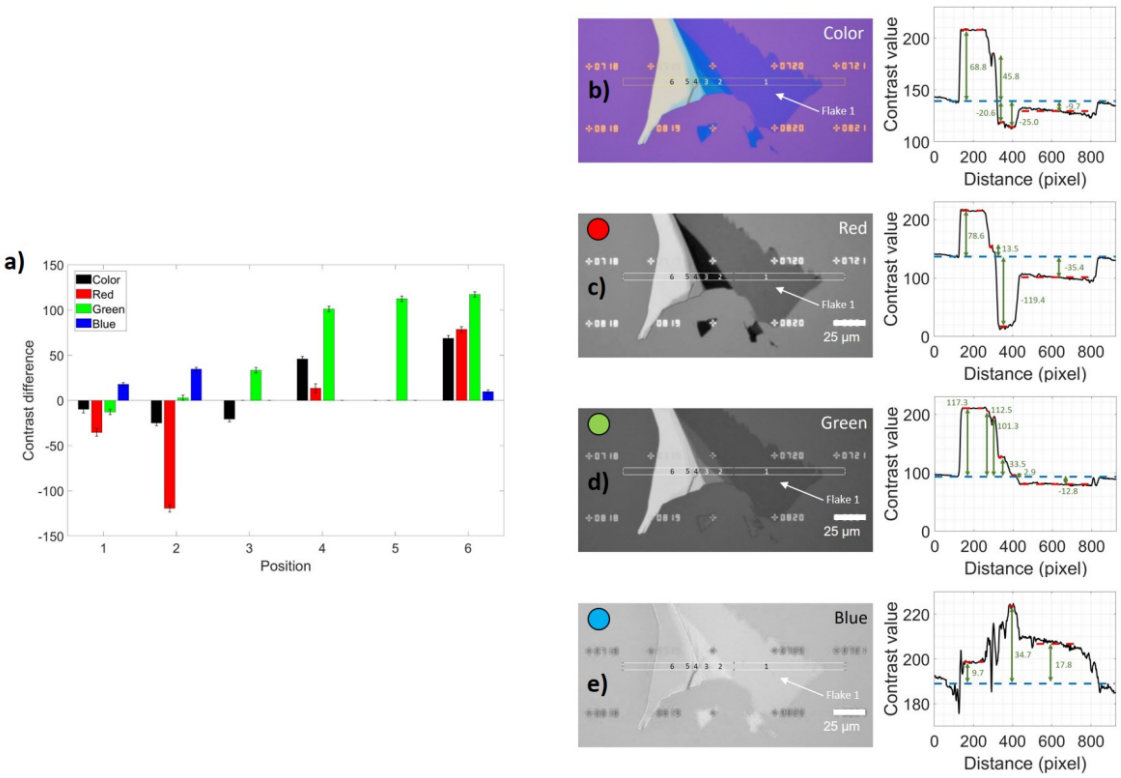

Figure 3.2. Micrograph images and contrast profiles of $MoSe_2$ flakes on 300 nm of SiO_2/Si. Contrast difference between the highlighted regions in b)-e) and the substrate are plotted in a). Figure reprinted from our previous work Cowie *et al.* (2021) with permission.

ers post-fabrication; however, our previous work - Cowie *et al.* (2021) - showed that some of these methods can often supply fundamentally disagreeing results with discrepancies in height measurements of exfoliated flakes of $MoSe_2$ on SiO_2. Techniques like photoluminescence spectroscopy (PL), X-ray photoelectron spectroscopy (XPS), Rutherford backscattering spectrometry (RBS), transmission electron microscopy (TEM), multiple-beam interferometry, and spectroscopic ellipsometry are also commonly used in the literature for classification. In this thesis, we look at and cross-reference optical contrast, amplitude modulation mode AFM, t-SPL topography, and Raman spectroscopy on different samples to estimate the number of layers of the flakes used before or after device fabrication.

OPTICAL CONTRAST

Optical contrast (OC) methods of TMDs on SiO_2/Si have been widely used to provide rapid,

non-destructive, and low-cost estimates of the layer count of samples ranging from single- to quindecuple-layer (1L - 15L) 2D nanosheets [H. Li *et al.*, 2013]. The thickness of the SiO_2 coating is chosen to make TMD flakes visible in optical microscopes using the optical interference of the air/TMD/SiO_2/Si multi-layer. The OC with respect to the substrate is directly measured from the optical image using the publicly-available ImageJ software. The contrast difference (C_D) is defined as the difference between the nanosheet (C) and the substrate (C_S) contrasts. Theoretical models for the optical contrast of graphene flakes predicted peaks to be at 90 or 300 nm of SiO_2 [Casiraghi *et al.*, 2007; Blake *et al.*, 2007]; while, similar values like 55 and 220 nm for MoS_2 monolayers were also observed [Late *et al.*, 2012]. For device applications, semiconductor flakes are usually deposited on 300 nm of SiO_2, as the insulating oxide layer bears a large breakdown voltage [Kasprzak, Laibowitz, and Ohring, 1977]. A Nikon (LV100ND) microscope with a "white" light source in a cleanroom environment with exposure times of 200 ms is used in this work to observe to OC of h-BN and WS_2 flakes on 300 nm ± 10% SiO_2/Si substrates. Observe the contrast profiles in Figure 3.2 for flakes of $MoSe_2$. Although the OC for WS_2 on 300 nm SiO_2/Si is not well-recorded in literature, comparing contrast data to available WSe_2 data from literature was sufficient proof for us to roughly differentiate 1, 2, 3L from the bulkier flakes. AFM methods provided us with more robust evidence of monolayer, bilayer, and trilayer identities. The OC method has considerable drawbacks for smaller flakes and has been shown on numerous occasions to be misleading, such as in Ottaviano *et al.* (2017), as the OC is not always a monotonic function of the layer count and significantly depends on the oxide coating thickness.

RAMAN SPECTROSCOPY

Raman spectroscopy is also widely used to characterize nanoscale materials due to its non-destructive nature at low operational intensities, user-friendly software and apparatuses, moderate lateral resolution, and sensitivity to material changes such as mechanical strain temperature gradients, doping, and defects. Regarding the characterization of WS_2 flakes, different

information can be acquired from Raman features (frequencies, linewidths, and intensities) of phonon and interlayer (layer breathing and shear) modes. In this work, we utilize a Renishaw Invia Raman Microscope with a diode pumped solid state laser excitation wavelength (λ_{exc}) of 532 nm at a 50 mW power and 120s exposure times; the measurement is conducted at ambient pressure and room temperature, and the beam spot size is roughly 1 μm in diameter.

Observe from the spectral data in Figure 3.3 that the frequencies of the out-of-plane phonon mode $A_{1g}(\Gamma)$, in-plane phonon mode $E^1_{2g}(\Gamma)$, and the longitudinal-acoustic mode LA(M) peaks can be deconvolved and roughly agree with those of Table 1 in Berkdemir *et al.* (2013) for 1-, 2-layer, and bulk WS_2 flakes. The $A_{1g}(\Gamma)$ modes for the flakes are at 414.7, 416.7, and 418.8 cm^{-1} for monolayer, bilayer, and bulk regions respectively. Berkdemir *et al.* (2013) do - however - report at a λ_{exc} of 514.5 nm that these Raman shifts would rather be at 417.2, 418.4, and 420.1 cm^{-1}. This discrepancy can likely be attributed to: the difference in fabrication techniques, as their sample is CVD-grown rather than mechanically exfoliated; size, alignment, and homogeneity of the sample surface as strain can have noticeable effects on the band structures of semiconductors; and potential tape residue or other contaminants present on the flake. Interestingly, PMGI polymer residue adhered to the substrate is traditionally observed in the bands at 1137, 1178, 1300, 1312, 1400, 1410, 1434, 1458, and 1604 cm^{-1} [Araujo *et al.*, 2019]; however, baseline-corrected Raman spectroscopy measurements on the device in Figure 3.3d feature flat bands of negligible intensities at these shifts indicating that very small amounts of residue content remain after the original bilayer lift-off process used in this thesis. The cumulative envelopes are formed by summing the individual curve fit paramters, which are themselves chosen from manual anchor points and adjusted over iterations to compute the best envelope fit. The correction was performed using a standard asymmetric least square smoothing baseline method. The measurements were analyzed using the OriginLab Pro 2024b software and Plotly graphing libraries. Altogether, Raman spectroscopy provided much insight on the classification of layers as well as surface material characterization; however, many complications arise in the identification of Raman shift peaks and comparison with literature as the combination of phonon modes, excitation wavelengths used, surface contaminants, strain effects, oxide layer

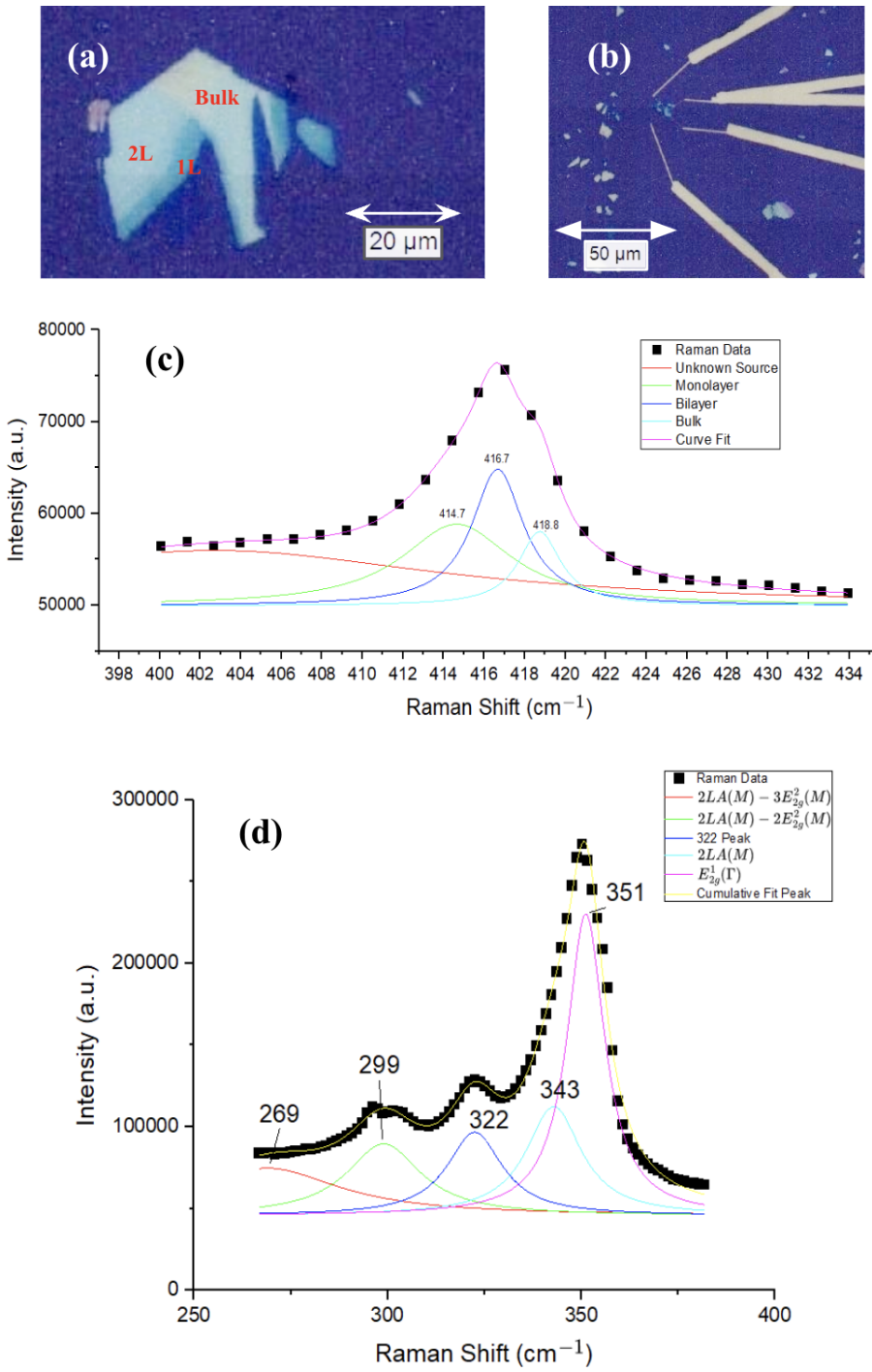

Figure 3.3. Raman spectroscopy measurements of mechanically exfoliated WS_2 samples placed on a 300 nm SiO_2/Si substrate. Optical micrographs of (a) 1L, 2L, and Bulk WS_2 crystals and (b) nanofabricated gold four-point probe few-layered WS_2 device. (c) Room-temperature Raman spectra from the flakes in the first sample deconvolved to locate the A_{1g} (Γ) modes for the monolayer, bilayer, and bulk regions. (d) Spectra of the first sample observing the deconvolution of the 2LA(M), $E^1_{2g}(\Gamma)$, and interlayer coupling phonon modes at 343, 351, and 299/322 cm^{-1} respectively. Overlapping spectra of the samples in (a) and (b) can be found in Appendix A. The SiO_2/Si peak can be observed at 519 cm^{-1}. Refer to Appendix A.3 for residuals and deconvolution fitting parameters. Results from Berkdemir *et al.* (2013) guided the identification of these peaks.

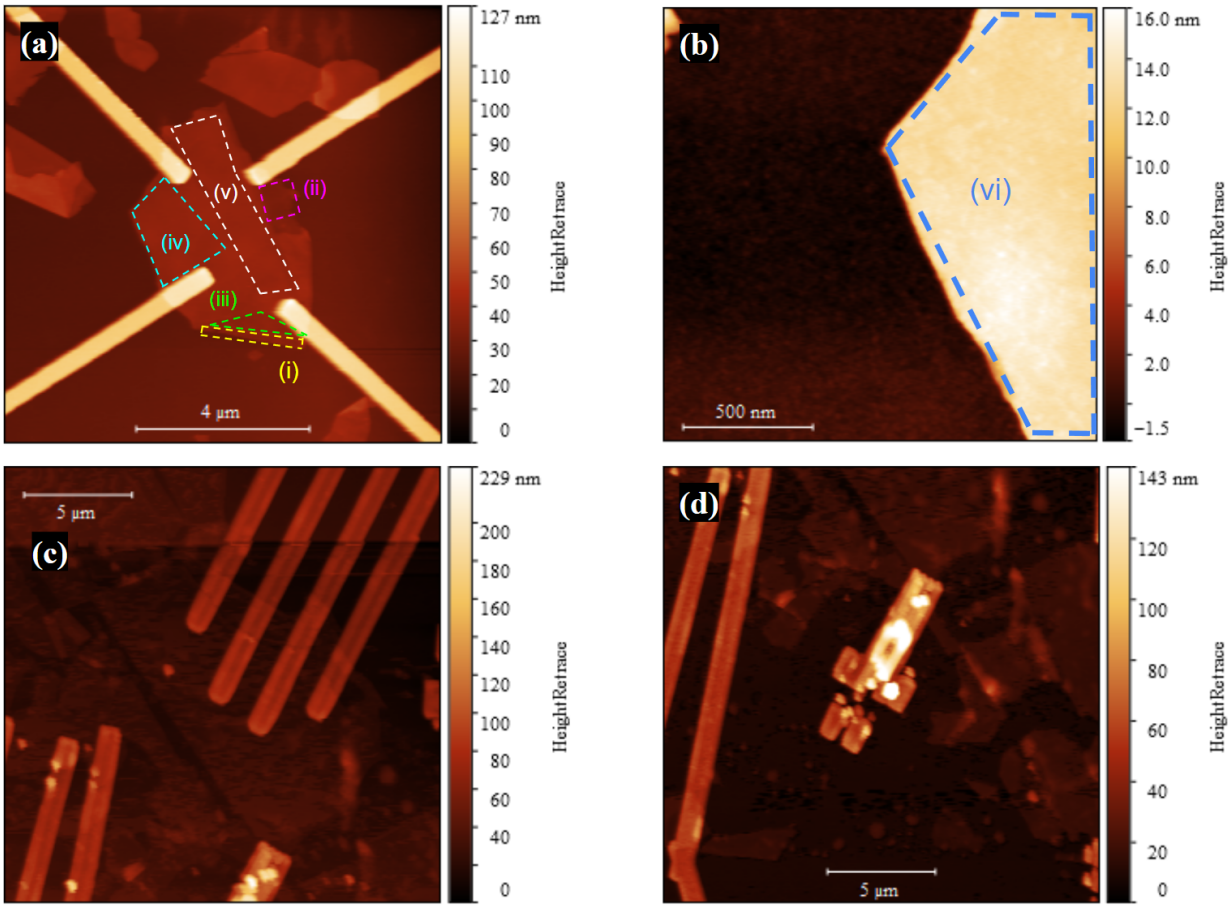

Figure 3.4. Amplitude Modulation Mode AFM topography channel scans of two WS_2 samples: (a,b) and (c,d). Scan (b) is a zoom on the left side of (a), within region (iv). Regions (i-v) and (vi) are selected to observe and compare different layers of the mechanically exfoliated flake. Scan (c) shows a 4PP device with 2 μm separation on a second sample, and scan (d) shows an attempted miniaturized 4PP device positioned nearby on that same flake with 200 nm separation.

thicknesses, and other complex parameters can affect the location of the peaks and intensities. Accurately classifying layers from the Raman spectroscopy of a single sample alone could be quite tricky.

AM-AFM

AFM is often used to measure the characteristic step height of a flake, which can be compared to the predicted interlayer spacing of the 2D nanosheet. There are significant discrepancies among the AFM step height measurements of mechanically exfoliated TMDs on SiO_2:

ranging from 0.6 ± 0.5 nm for WS_2 [Paolucci *et al.*, 2019] to 6.5 ± 1.5 nm for $MoSe_2$ [Cowie *et al.*, 2021] depending on the technique. It has been shown that step heights for the same flakes measured in amplitude modulation mode (AM) and nc-AFM can be significantly higher than in techniques like kelvin probe force microscopy (KPFM) where electrostatic forces are compensated for [Cowie *et al.*, 2021]. However, amplitude modulation mode operates at a larger tip-sample force regime than KPFM and nc-AFM, so it can mechanically influence (e.g. compress) the sample, overlayer, underlayer, or general interlayer liquids, gases, and contaminants.

In this thesis, we utilize amplitude modulation mode AFM to measure the thickness of our flakes. The WS_2 layers were exfoliated mechanically using the original method described in Figure 3.1 onto 300 nm SiO_2/Si. Amplitude modulation mode measurements were performed in air and at room-temperature with a MFP-3D (BIO) Asylum instrument using 240AC-PP conducting OPUS tips with 1-2 Nm^{-1} spring constants and oscillations amplitudes between 14 and 16 nm. The setpoint was 0.75 V or 75 percent of the free vibrational amplitude to ensure "soft" tapping. The scan was conducted at a speed of 0.2 Hz - one line every 5 sec - at 512 points per line.

For the AFM data, step heights are measured by average over considerable surface areas rather than individual line profiles, as the rough TMD surfaces can result in hugely different profiles across their boundaries. The raw data is first sent through some preliminary image-processing tools: we level the z-channel by mean plane subtraction and by means of making facets point upwards in order to ensure that the substrate is equal to the measurement noise, align the rows using a median of differences method, correct horizontal scaring, then manually level any drooping in the SiO_2 substrate. Masked regions of homogenous substrate and TMD surfaces are then carefully selected to produce histograms or the measured layers, as shown in Appendix A.4. It was observed that the Lorentzian distribution function of the form $f(x) = y_0 + \frac{a}{b^2+(x-x_0)^2}$ provided better curves of best fit to the height distribution histograms. Uncertainties from the regions in Figure 3.4(a and b) are calculated by adding the Lorentzian half FWHMs in quadrature as $\delta h = \sqrt{(\sigma^2_{sample} + \sigma^2_{substrate})}$, developed by Dr. Cowie in Cowie *et al.* (2021).

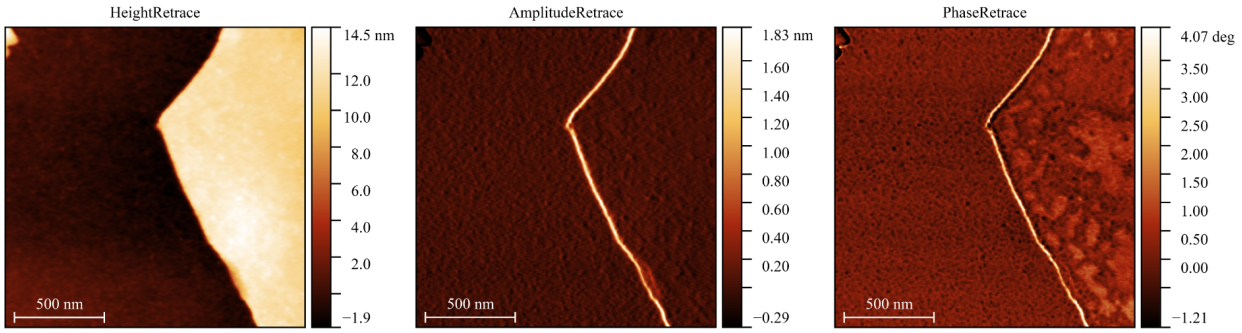

Figure 3.5. Height, amplitude, and phase channels of a WS_2 flake on SiO_2. The phase channel provides a contrast mechanism to study changes in material properties. Some contrast is visible potentially indicating tape residue, oxidation, water content, or other contaminants on the semiconductor surface that were previously invisible in the topography channel.

Using this technique, we were able to measure that the substrate resides at a z-position of 0.0 with a $\sigma_{substrate-A}$ of 1.5 nm in (a) and $\sigma_{substrate-B}$ of 0.4 nm in (b). At the labeled masks in (a), we can observe terraces residing at: (i) 9.6 ± 1.6 nm, (ii) 9.9 ± 1.8 nm, (iii) 11.1 ± 1.6 nm, (iv) 15.7 ± 1.75 nm, and (v) 17.8 ± 1.7 nm; at the masked region of (b), we measure the terrace at (vi) 12.4 ± 0.6 nm. Interestingly, the same step feature on the left side of Figure 3.4a and 3.4b measures at 15.7 ± 1.75 nm and 12.5 ± 0.6 nm respectively, in disagreement with each other beyond error. This indicates that the same sample, using the same instrument and measuring parameters can result in significantly different step heights. Based on the measured plateau regions and supplementary line profiles, we observe a monolayer step at the bottom of the flake with a measured height of 1.5 ± 2.3 nm. Although, this is not in agreement with the literature, we have mentioned numerous AFM-related factors that may affect this discrepancy.

Combining the height channel with data from the phase and amplitude channels can also serve as a powerful tool for studying the nanomechanical properties of 2D flakes as seen in Figure 3.5. On top of the excellent vertical resolution of AFM, it is also extremely useful in measuring the lateral spatial differences between features. As shown in Figure 3.4(c and d), AM-AFM can be used to verify the separation between probes as well as the size of flakes and features under the diffraction limit.

T-SPL TOPOGRAPHY

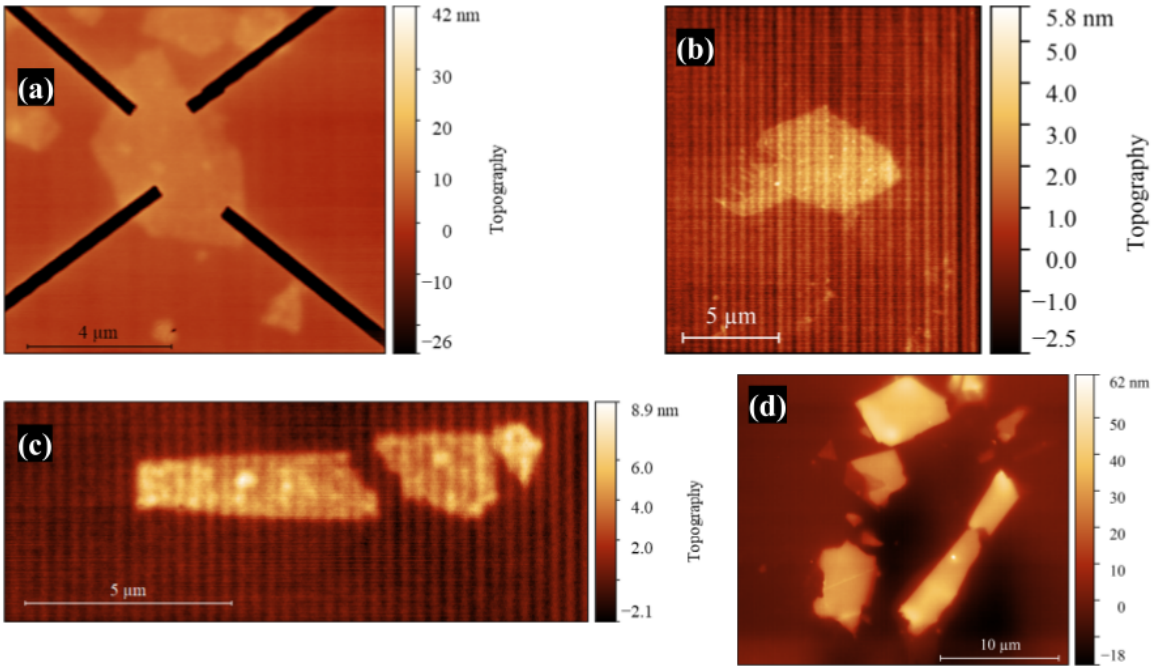

Figure 3.6. T-SPL Topography images of various WS_2 samples under roughly 90 nm (a-c) and 200 nm (d) of PPA/PMGI polymer resist. Vertical stripes in (b) and (c) can likely be attributed to fast scan speed feedback oscillations. Note that a single flake like the one observed in (a) that has been imaged in an AFM system can also conveniently be optically observed and imaged in a t-SPL system.

Although the primary utility of t-SPL instruments is lithography for nanofabrication, this method has proven to hold fascinating imaging capabilities like observing nanoscale objects and features under large amounts of polymer resist. This is absolutely necessary for the accurate placement of nanoscale contacts and patterns onto the flakes and substrate. These "topography" scans in Figure 3.6 are measured under 55 nm of PMGI SF 2 and 35 nm of PPA, or a total of 90 nm of polymer resist. Measurements were conducted on a Nanofrazor Explore system at ambient pressure and room-temperature, in a cleanroom environment. The working principle and method for this imaging process is discussed in Chapter 3.

In 3.6a, we re-observe the previously studied WS_2 device. We can compare the AM-AFM terraces to the topography measured via T-SPL. Using the same histogram technique as in the AFM section, shown in Appendix A.4, we measure the "substrate" - or technically the overlayer PPA - to be at position of 0.0 nm with a $\sigma_{foreground}$ of 1.3 nm. Due to limited contrast in the

topography image, we can only accurately select two of the masks to compare to AM-AFM data: the left-side of the flake, which is the same region as (iv) and (vi), and a center piece - the same region as (v) in the AM-AFM experiment. T-SPL data for the left corner of the flake indicates a terrace at 6.9 ± 1.5 nm, which is substantially lower - less than half - of the AM-AFM measurement for that region. Similarly, t-SPL data for the center piece of the flake feature a terrace at 8.1 ± 1.5 nm, which is also nearly half of the corresponding AM-AFM data. This is not entirely surprising, as the contrast mechanisms for t-SPL and AM-AFM are fundamentally different; t-SPL measures heat conductivity, while AM-AFM measures topography. Two data points may be insufficient to call a trend, but this is a recurring theme throughout the thesis with flakes appearing much thinner than in reality in sub-resist topography data. This was also observed as optically murkier (bulk) flakes falsely appearing to be few-layered nanosheets in t-SPL data. The relationship between flake thickness and heat conductivity is not entirely understood and any discrepancies can likely be attributed to heat dissipation and resist thickness-dependent thermal conductivity effects. It would be useful to be able to identify monolayer samples and distinguish them using thermal scanning probe microscopy, as it would avoid an extra characterization step by AM-AFM.

We can also observe in Figures 3.6 (b) and (c) that the vertical resolution for topography allows for the identification of nanoscale features. Figure (d) is also an excellent example of the technique's ability to rapidly read large-scale surfaces at high precision, as the image took roughly 3 min to produce under 200 nm of resist. The flake in figure (b) indicates two peaks at: 0.57 and 2.0 nm. From this topography data alone, one would predict the flake to be 1L and 4L WS_2. Clearly, however, we've demonstrated above that t-SPL topography data alone can be deceptive and is not sufficient to accurately classify the layer count of flakes on SiO_2/Si substrate.

None of these techniques alone would be a safe bet to classify the number of layers present in a flake or nanosheet. At least two or more must be used in conjunction to confidently classify layers with the most reliable combination being AFM and optical techniques like Raman and PL spectroscopy.

3.2 Electrical Characterization Device Architectures

The atomic thickness of 2DMs enable highly scaled field-effect transistors (FETs) with the advantage of reduced short-channel effects and high carrier-mobilities, optimizing low-voltage, high-performance operations. Accurate characterization of the device parameters of 2D FETs such as carrier density, mobility, resistivity, contact resistance, charge trap densities, anisotropy in carrier transport, and dielectric permittivity are mandatory to quantifying the ultimate performance of devices. Semiconductor device performance research primarily focuses on improving the ON/OFF ratio, conductivity, carrier mobility, and power consumption metrics [Schwierz, 2010; Chhowalla, Jena, and H. Zhang, 2016; Mitta *et al.*, 2020]. The use of conventional characterization methods can produce deceptive results when applied to 2D vdw materials, as certain metrics like charge carrier density - for instance - behave fundamentally differently in 2D materials than in the bulk [Kiriya *et al.*, 2014]. As such, variations or novel techniques must be considered.

The pristine 2D surfaces tend to form weak vdW bonds with adjacent materials such as metal-semiconductor junctions, preventing the creation of low-resistance contacts. The transport of charge carriers is then hindered by tunnel barriers at the interface, defect-induced interface states, and orbital overlap; these are often prone to Fermi level-pinning. As a result, it is useful to study the naturally-occurring Schottky-barrier height to better understand contact resistance [X. Liu *et al.*, 2022]. In this work, we fabricate popular electrical characterization architectures with the aim of studying conductivity, Schottky-barrier height, and contact resistance in 2D WS_2 FETs.

3.2.1 Conductivity (Resistivity)

The basic structure of an FET comprises of a semiconductor channel between source (S) and drain (D) electrodes, a metallic gate, and an insulating gate oxide between the channel and gate. The drain current flowing in the SD channel can be established by the source-drain voltage (V_{SD}) and modulated by the applied gate voltage (V_G), which increases or decreases the conductivity of the channel. In the case of the devices fabricated in this thesis, the circuit involves a typical back-gated 2D FET layout with the 300 nm SiO_2 serving as the insulator requiring large gate voltages (e.g. >10V) to switch the devices from the OFF to ON configurations. It would have been nice to instead stack the WS_2 on an thin h-BN insulating layer and onto a graphene gate for easier gating.

Conductivity in isotropic bulk materials can be easily made using standard multi-point resistance measurements; however, the fragile and confined nature of 2D materials make these experiments difficult. Some non-invasive techniques like four-probe STM are being developed to circumvent the nanofabrication-related difficulties in characterization experiments [A.-P. Li *et al.*, 2013; Miccoli *et al.*, 2015]. Many thicker flakes have been demonstrated to follow super-linear behaviour ($\sigma \propto t^{-k}$) of electrical conductivity with respect to sample thickness [Siao *et al.*, 2018]. Large inter-sample variation due to doping from defects, ambient gas, and sample preparation methods can make these experiments particularly challenging for quantitative reproducibility. It has however been observed that t-SPL-fabricated devices result in substantially less invasive doping and topographic damage than EBL-fabricated devices, exceptionally allowing for vanishing Schottky barrier heights (around 0 meV) and ON/OFF-ratios of 10^{10} [Zheng *et al.*, 2019]. These devices also exhibit much higher mobilities and charge densities due to less induced defects and trapped charges. As a result, the most straightforward way of quantifying conductivity or resistivity in 2D (roughly < 10 layers) is in terms of channel resistance (R_{CH}) and sheet resistance (R_{SH}).

Traditionally, however, the contact resistance in back-gated 2D FET devices can be comparable or even larger than channel resistance, resulting in considerable errors in R_{CH} [H. Liu, Neal,

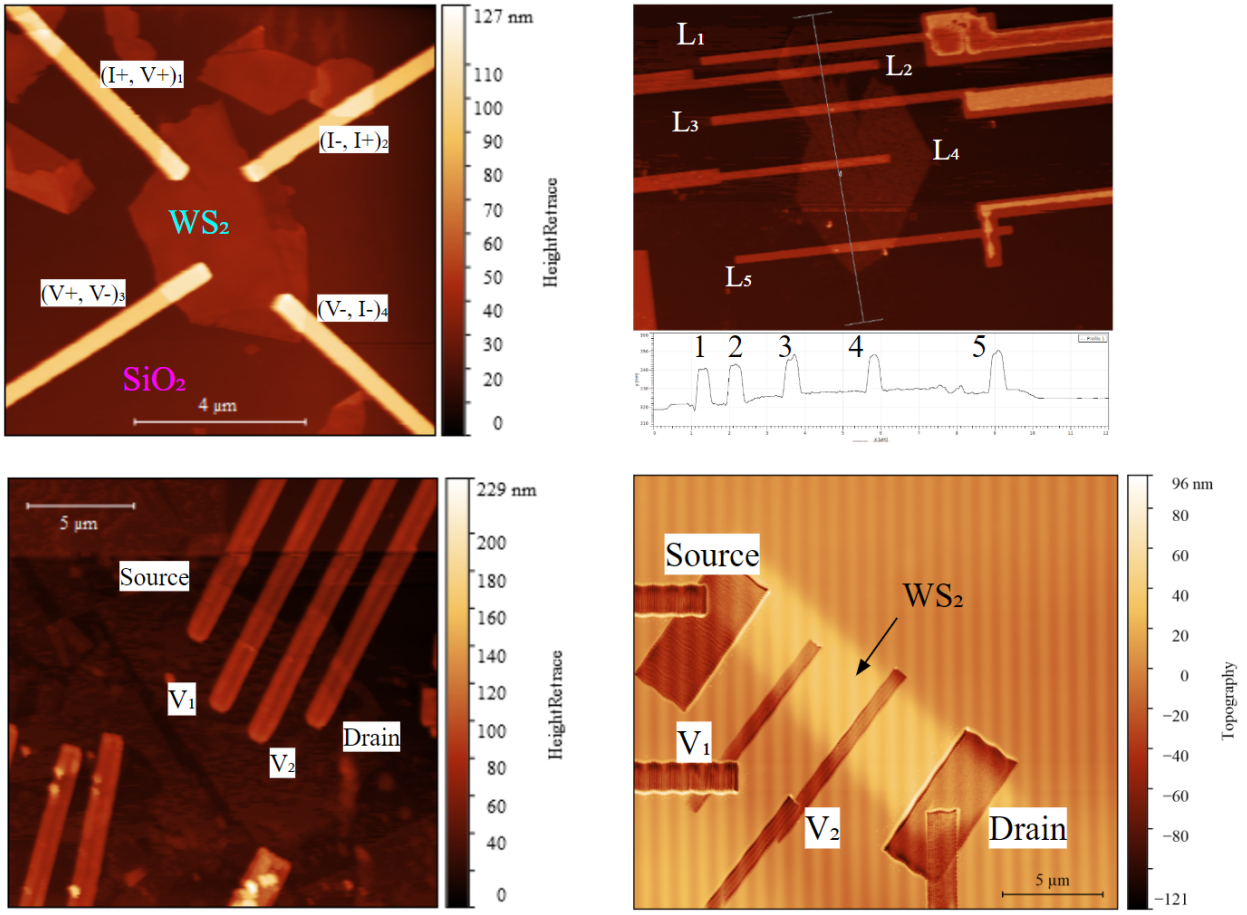

Figure 3.7. Top-Left: Van der Pauw Method (AM-AFM Height), Top-Right: Transfer Length Method (AM-AFM Height), Bottom-Left: Equal-Separation Four-Point Probe (4PP) Method (AM-AFM Height), Bottom-Right: 4PP Device with a Hall bar geometry (tSPL Topography)

and Ye, 2012]; this can be solved using 4PP devices instead, which deconvolutes the effect of R_C on R_{CH} and R_{SH} measurements [J. I.-J. Wang *et al.*, 2015]. As observed in Figure 3.7(TL and BR), we fabricated 4PP devices in two distinct architectures allowing for the measurements of R_{CH} independent of the contact resistance R_C, which can often be a large and impeding factor in 2D devices.

4PP in HALL BAR GEOMETRIES

In the Hall bar geometry, the voltage probes V_1 and V_2 ($V_{12} = |V_2 - V_1|$) negligibly affect the surrounding current channel flow I_D from source to drain and act like ideal voltmeters. R_{CH} can then be extracted from the IV-curves following the relation

$$R_{CH} = R_{SH}\frac{L}{W} = \frac{1}{\sigma \cdot t_{CH}} \cdot \frac{L}{W} \quad \text{and} \quad R_{CH} = \frac{V_{12}}{I_D}\frac{L}{L_{12}} \tag{3.1}$$

where L is the distance from the source to the drain ($11.35 \pm 5 \times 10^{-2}$ μm), L_{12} is the distance from V_1 to V_2 ($5.00 \pm 5 \times 10^{-2}$ μm), W is the width of the channel ($6.82 \pm 5 \times 10^{-2}$ μm), and t_{CH} is the thickness of the semiconductor component of the device (38 ± 4 nm) using a method for calculating vertical uncertainty similar to the quadrature sum described previously. Subtracting R_{CH} from the total resistance can then provide a more accurate estimate of the contact resistance while still providing a measurement of intrinsic conductivity.

4PP in VAN DER PAUW GEOMETRIES

As mechanically exfoliated 2D flakes often come in irregular shapes and the use of milling, reshaping, or nanocutting instruments can be costly, it may be easier to produce 4PP measurements with van der Pauw rather than Hall bar geometries. The van der Pauw method allows four contacts to be places at the periphery of a flake as shown in the TL figure above in an arrangement of configurations. The current can flow from 1-2 or 2-4 while the voltage drops are recorded using the adjacent 3-4 or 1-3 probes. The resistances can then be calculated using the

Vertical Configuration (X):

$$R_{12,34} = \frac{V_{34}}{I_{12}}, \qquad R_{21,43} = \frac{V_{43}}{I_{21}}, \qquad R_{34,12} = \frac{V_{12}}{I_{34}}, \qquad R_{43,21} = \frac{V_{21}}{I_{43}} \tag{3.2}$$

Horizontal Configuration (Y):

$$R_{13,24} = \frac{V_{24}}{I_{13}}, \qquad R_{31,42} = \frac{V_{32}}{I_{31}}, \qquad R_{24,13} = \frac{V_{13}}{I_{24}}, \qquad R_{42,31} = \frac{V_{31}}{I_{42}} \tag{3.3}$$

Resistances may then be averaged as such

$$R_X = \frac{(R_{12,34} + R_{21,43} + R_{34,12} + R_{43,21})}{4} \tag{3.4}$$

$$R_Y = \frac{(R_{13,24} + R_{31,42} + R_{24,13} + R_{42,31})}{4} \tag{3.5}$$

to produce a relation that combines sheet resistance and conductivity:

$$e^{-\pi R_X/R_{SH}} + e^{-\pi R_Y/R_{SH}} = 1 \quad \text{and} \quad \sigma = \frac{1}{R_{SH} \cdot t_{CH}} \tag{3.6}$$

where σ is conductivity and t_{CH} is the known thickness of the semiconductor flake (from AFM measurements). In the case of our flake, the thickness is 15.7 ± 1.75 nm in the vicinity of the probed region.

3.2.2 Contact Resistance

The lack of straightforward and controllable doping techniques for 2DMs results in high R_C metal-semiconductor junctions. The contact resistance tends to depend on the barrier dimensions, affecting the carrier transport across it. Traditional SC devices made of Si and GaAs commonly approach the quantum limit for R_C [Russo *et al.*, 2010]. Few-layered TMD and semiconductors with large band gaps (0.6 - 2 eV), however, show larger contact resistances - over 10 times that of conventional devices - due to the formation of Schottky barriers from middle band gap FLP; these are commonly observed to be a result of intrinsic defects and processing conditions [Y. Xu *et al.*, 2016; Y. Liu *et al.*, 2018]. Picking high work function metals for the junctions can result in weak vdW bonding and therefore large tunnel and contact resistances. For this reason, we chose titanium (Ti) (4.2 eV) instead of chromium (Cr) (4.5 eV) as our adhesive layer between the highly conductive gold (Au) (5.2 eV) metal and WS_2 semiconductor. This additionally allows the Ti to form bonds with SiO_2 and serve as an adhesive layer; whereas, the Au films would not structurally adhere to the substrate.

As seen in the TR figure above, we built a device based on the most popular architecture and

method of measuring contact resistance - the transfer length method (TLM), also known as the transmission line method. The total resistance R_tot can be expressed as a linear combination of the R_C and the length-dependent R_{CH} between any two contacts such as

$$R_{tot} = R_{CH} \cdot (L) + 2R_C \quad \text{or} \quad R_{tot} \cdot W = R_{SH} \cdot L + 2R_C \cdot W \tag{3.7}$$

Plotting the cumulative total resistance along the device at $L_1, L_2, \cdots, L_5$ along the channel length follows the linear behaviour in Equation 3.7 which indicates that the y-intersect is equal to $2R_C$. Using AM-AFM, we were able to accurately measure the channel lengths, heights, widths, and separations as seen in the profile line in Figure 3.7. These provide generally simple and effective means of measuring these metrics.

We were unable to produce IV curves and resistance measurements for the devices built, as two devices experienced electrical breakdown due to high current loads (in the mA regime) and another device's fragile 25nm-thick Au/Ti contact pads were torn off by overpowered wire-bonding sonic pulses.

4 Conclusion & Outlook

In this work, we developed methodology for the nanofabrication of 2D TMD devices using thermal scanning probe lithography (t-SPL). We were able to leverage ultra-thin PMGI and PPA films around 30 and 10 nm respectively to pattern at high resolutions (sub-40nm) patterns and electrical contacts on few-layered WS_2 flakes in various device architectures.

We successfully identified and solved a multitude of nanofabrication-related issues such as UV laser-dosage, capillary force, and over-development related issues in this bilayer liftoff process. Fundamental discrepancies between t-SPL topography and TM-AFM as well as disagreeing AM-AFM measurements in layer counts and thicknesses were also discovered and quantified. This illustrates the necessity for combining multiple characterization methods to classify the layer counts of semiconductor flakes.

In the future, it would be interesting to see if layer counts of flakes can be optically characterized under thin polymer resists. It would also be useful to be able to identify monolayer samples and distinguish them using thermal scanning probe microscopy, as it would avoid an extra characterization step by AM-AFM.

BIBLIOGRAPHY

Achal, Roshan *et al.* (July 2018). "Lithography for robust and editable atomic-scale silicon devices and Memories". In: *Nature Communications* 9.1. DOI: 10.1038/s41467-018-05171-y.

Araujo, Eduardo Nery de *et al.* (Feb. 2019). "Effects of post-lithography cleaning on the yield and performance of CVD graphene-based devices". In: *Beilstein Journal of Nanotechnology* 10, pp. 349–355. DOI: 10.3762/bjnano.10.34.

Aso, Chuji, Sanae Tagami, and Toyoki Kunitake (Feb. 1969). "Polymerization of aromatic aldehydes. II. Cationic cyclopolymerization of phthalaldehyde". In: *Journal of Polymer Science Part A-1: Polymer Chemistry* 7.2, pp. 497–511. DOI: 10.1002/pol.1969.150070208.

Berkdemir, Ayse *et al.* (Apr. 2013). "Identification of individual and few layers of WS2 using Raman spectroscopy". In: *Scientific Reports* 3.1. DOI: 10.1038/srep01755.

Binnig, G., C. F. Quate, and Ch. Gerber (Mar. 1986). "Atomic Force Microscope". In: *Physical Review Letters* 56.9, pp. 930–933. DOI: 10.1103/physrevlett.56.930.

Binning, G. *et al.* (1982). "Surface studies by scanning tunneling microscopy". In: *Scanning Tunneling Microscopy*, pp. 31–35. DOI: 10.1007/978-94-011-1812-5_1.

Blake, P. *et al.* (Aug. 2007). "Making graphene visible". In: *Applied Physics Letters* 91.6. DOI: 10.1063/1.2768624.

Bussmann, E. *et al.* (Aug. 2021). "Atomic-Precision Advanced Manufacturing for quantum computing." In: *Proposed for presentation at the Materials Science for Quantum Computing in ,* DOI: 10.2172/1889038.

Bustamante, José *et al.* (2024). *Needle in a haystack: efficiently finding atomically defined quantum dots for electrostatic force microscopy*. arXiv: 2403.13935 [cond-mat.mes-hall].

Casiraghi, C. *et al.* (Aug. 2007). "Rayleigh imaging of graphene and graphene layers". In: *Nano Letters* 7.9, pp. 2711–2717. DOI: 10.1021/nl071168m.

Chen, J. Fung *et al.* (Mar. 2008). "Development of a computational lithography roadmap". In: *Optical Microlithography XXI*. DOI: 10.1117/12.773060.

Chen, W. *et al.* (Sept. 1999). "Disappearance of the Kondo resonance for atomically fabricated cobalt dimers". In: *Physical Review B* 60.12. DOI: 10.1103/physrevb.60.r8529.

Chhowalla, Manish, Debdeep Jena, and Hua Zhang (Aug. 2016). "Two-dimensional semiconductors for transistors". In: *Nature Reviews Materials* 1.11. DOI: 10.1038/natrevmats.2016.52.

Chou, Stephen Y., Peter R. Krauss, and Preston J. Renstrom (Nov. 1996). "Nanoimprint lithography". In: *Journal of Vacuum Science amp; Technology B: Microelectronics and Nanometer Structures Processing, Measurement, and Phenomena* 14.6, pp. 4129–4133. DOI: 10.1116/1.588605.

Conley, Will *et al.* (June 1990). "Negative tone aqueous developable resist for photon, electron, and X-ray lithography". In: *SPIE Proceedings*. DOI: 10.1117/12.20087.

Coulembier, Olivier *et al.* (2009). "Probe-based nanolithography: Self-amplified depolymerization media for dry lithography". In: *Macromolecules* 43.1, pp. 572–574. DOI: 10.1021/ma9019152.

Cowie, Megan *et al.* (Dec. 2021). "How high is a mose2 monolayer?" In: *Nanotechnology* 33.12, p. 125706. DOI: 10.1088/1361-6528/ac40bd.

Crommie, M. F., C. P. Lutz, and D. M. Eigler (Oct. 1993). "Confinement of electrons to quantum corrals on a metal surface". In: *Science* 262.5131, pp. 218–220. DOI: 10.1126/science.262.5131.218.

Dagata, J. A. *et al.* (May 1990). "Modification of hydrogen-passivated silicon by a scanning tunneling microscope operating in Air". In: *Applied Physics Letters* 56.20, pp. 2001–2003. DOI: 10.1063/1.102999.

Dransfeld, K. and J. Xu (1988). "The heat transfer between a heated tip and a substrate: Fast thermal microscopy". In: *Journal of Microscopy* 152.1, pp. 35–42. DOI: 10.1111/j.1365-2818.1988.tb01359.x.

Duan, Huigao *et al.* (Nov. 2010). "Metrology for electron-beam lithography and resist contrast at the sub-10 nm scale". In: *Journal of Vacuum Science amp; Technology B, Nanotechnology and Microelectronics: Materials, Processing, Measurement, and Phenomena* 28.6. DOI: 10.1116/1.3501359.

Dwyer, K. J., Michael Dreyer, and R. E. Butera (Nov. 2019). "STM-induced desorption and lithographic patterning of cl–si(100)-(2 × 1)". In: *The Journal of Physical Chemistry A* 123.50, pp. 10793–10803. DOI: 10.1021/acs.jpca.9b07127.

EIA (2019). *Appendix C*. URL: https://www.eia.gov/electricity/monthly/pdf/technotes.pdf.

Eigler, D. M. and E. K. Schweizer (Apr. 1990). "Positioning single atoms with a scanning tunnelling microscope". In: *Nature* 344.6266, pp. 524–526. DOI: 10.1038/344524a0.

El Garah, Mohamed *et al.* (May 2018). "Mos2 nanosheets via electrochemical lithium-ion intercalation under ambient conditions". In: *FlatChem* 9, pp. 33–39. DOI: 10.1016/j.flatc.2018.06.001.

Feynman, Richard P. (1959). "There's Plenty of Room at the Bottom". In.

Fuechsle, Martin *et al.* (Feb. 2012). "A single-atom transistor". In: *Nature Nanotechnology* 7.4, pp. 242–246. DOI: 10.1038/nnano.2012.21.

Garcia, Ricardo, Armin W. Knoll, and Elisa Riedo (Aug. 2014). "Advanced scanning probe lithography". In: *Nature Nanotechnology* 9.8, pp. 577–587. DOI: 10.1038/nnano.2014.157.

Garcia, Ricardo, Ramses V. Martinez, and Javier Martinez (2006). "Nano-chemistry and scanning probe nanolithographies". In: *Chem. Soc. Rev.* 35.1, pp. 29–38. DOI: 10.1039/b501599p.

Gartside, Jack C. *et al.* (Nov. 2017). "Realization of ground state in artificial kagome spin ice via topological defect-driven magnetic writing". In: *Nature Nanotechnology* 13.1, pp. 53–58. DOI: 10.1038/s41565-017-0002-1.

Gmelin, E, R Fischer, and R Stitzinger (1998). "Sub-micrometer thermal physics – an overview on sthm techniques presented at the twelfth Ulm-Freiberg Conference, Freiberg, Germany, 19–21 March 19971". In: *Thermochimica Acta* 310.1–2, pp. 1–17. DOI: 10.1016/s0040-6031(97)00379-1.

Grütter, P. *et al.* (Nov. 1987). "Observation of magnetic forces by the Atomic Force Microscope". In: *Journal of Applied Physics* 62.10, pp. 4293–4295. DOI: 10.1063/1.339105.

Hirayama, Yoshiro and Hiroshi Okamoto (Dec. 1985). "Electrical properties of ga ion beam implanted GaAs Epilayer". In: *Japanese Journal of Applied Physics* 24.12A. DOI: 10.1143/jjap.24.l965.

Ho, Yen-Hung, Yi-Hua Wang, and Hong-Yi Chen (Apr. 2014). "Magnetoelectronic and optical properties of a MoS_2 monolayer". In: *Phys. Rev. B* 89 (15), p. 155316. DOI: 10.1103/PhysRevB.89.155316. URL: https://link.aps.org/doi/10.1103/PhysRevB.89.155316.

Höflich, Katja *et al.* (Dec. 2023). "Roadmap for focused Ion Beam Technologies". In: *Applied Physics Reviews* 10.4. DOI: 10.1063/5.0162597.

Huff, Taleana *et al.* (Dec. 2018). "Binary atomic silicon logic". In: *Nature Electronics* 1.12, pp. 636–643. DOI: 10.1038/s41928-018-0180-3.

ITA (2024). *Morocco - Energy*. URL: https://www.trade.gov/country-commercial-guides/morocco-energy.

Ito, Hiroshi, Mitsuru Ueda, and Reinhold Dr Schwalm (1988). "Highly sensitive thermally developable positive resist systems". In: *Journal of Vacuum Science & Technology B* 6, pp. 2259–2263. URL: https://api.semanticscholar.org/CorpusID:97982642.

Ito, Hiroshi, C. Grant Willson, and Jean H. J. Frechet (1982). "New UV Resists with Negative or Positive Tone". In: *1982 Symposium on VLSI Technology. Digest of Technical Papers*, pp. 86–87.

Jaschke, Manfred and Hans-Juergen Butt (Apr. 1995). "Deposition of organic material by the tip of a scanning force microscope". In: *Langmuir* 11.4, pp. 1061–1064. DOI: 10.1021/la00004a004.

Jawaid, Ali *et al.* (Dec. 2015). "Mechanism for liquid phase exfoliation of MoS2". In: *Chemistry of Materials* 28.1, pp. 337–348. DOI: 10.1021/acs.chemmater.5b04224.

Kaestner, M. and I.W. Rangelow (Sept. 2012). "Scanning probe nanolithography on Calixarene". In: *Microelectronic Engineering* 97, pp. 96–99. DOI: 10.1016/j.mee.2012.05.042.

Kasprzak, L. A., R. B. Laibowitz, and M. Ohring (Oct. 1977). "Dependence of the si-sio2 barrier height on SIO2 thickness in MOS tunnel structures". In: *Journal of Applied Physics* 48.10, pp. 4281–4286. DOI: 10.1063/1.323415.

Kawai, Shigeki *et al.* (July 2014). "Atom manipulation on an insulating surface at room temperature". In: *Nature Communications* 5.1. DOI: 10.1038/ncomms5403.

Kayaku (2002). *Lor and PMGI resists for bi-layer lift-off processing*. URL: https://kayakuam.com/wp-content/uploads/2023/06/KAM-LOR-PMGI-Datasheet-4.30.24-final-1.pdf.

Kim, Yongshin and Sungho Rho (Feb. 2024). "The US–china chip war, Economy–Security Nexus, and Asia". In: *Journal of Chinese Political Science*. DOI: 10.1007/s11366-024-09881-7.

Kiriya, Daisuke *et al.* (May 2014). "Air-stable surface charge transfer doping of MOS2 by benzyl viologen". In: *Journal of the American Chemical Society* 136.22, pp. 7853–7856. DOI: 10.1021/ja5033327.

Krull, A. *et al.* (Mar. 2020). "Artificial-intelligence-driven scanning probe microscopy". In: *Communications Physics* 3.1. DOI: 10.1038/s42005-020-0317-3.

Lai, J. *et al.* (1995). "Thermal detection of device failure by atomic force microscopy". In: *IEEE Electron Device Letters* 16.7, pp. 312–315. DOI: 10.1109/55.388718.

Late, Dattatray J. *et al.* (Feb. 2012). "Rapid characterization of ultrathin layers of chalcogenides on SIO2/si substrates". In: *Advanced Functional Materials* 22.9, pp. 1894–1905. DOI: 10.1002/adfm.201102913.

Lee, J.-H. and Y. B. Gianchandani (May 2004). “High-resolution scanning thermal probe with servocontrolled interface circuit for microcalorimetry and other applications”. In: *Review of Scientific Instruments* 75.5, pp. 1222–1227. DOI: 10.1063/1.1711153.

Li, Hai *et al.* (Oct. 2013). “Rapid and reliable thickness identification of two-dimensional nanosheets using optical microscopy”. In: *ACS Nano* 7.11, pp. 10344–10353. DOI: 10.1021/nn4047474.

Li, M.-H and Y.B Gianchandani (May 2003). “Applications of a low contact force polyimide shank bolometer probe for chemical and Biological Diagnostics”. In: *Sensors and Actuators A: Physical* 104.3, pp. 236–245. DOI: 10.1016/s0924-4247(03)00026-8.

Li, An-Ping *et al.* (Mar. 2013). “Electron transport at the nanometer-scale spatially revealed by four-Probe Scanning Tunneling Microscopy”. In: *Advanced Functional Materials* 23.20, pp. 2509–2524. DOI: 10.1002/adfm.201203423.

Li, Yangang *et al.* (Dec. 2022). “Recent progress on the mechanical exfoliation of 2D transition metal dichalcogenides”. In: *Materials Research Express* 9.12, p. 122001. DOI: 10.1088/2053-1591/aca6c6.

Liu, Han, Adam T. Neal, and Peide D. Ye (Sept. 2012). “Channel length scaling of MOS2 mosfets”. In: *ACS Nano* 6.10, pp. 8563–8569. DOI: 10.1021/nn303513c.

Liu, Xiaochi *et al.* (Feb. 2022). “Fermi level pinning dependent 2D semiconductor devices: Challenges and prospects”. In: *Advanced Materials* 34.15. DOI: 10.1002/adma.202108425.

Liu, Yuan *et al.* (May 2018). “Approaching the schottky–mott limit in van der waals metal–semiconductor junctions”. In: *Nature* 557.7707, pp. 696–700. DOI: 10.1038/s41586-018-0129-8.

Lyding, J. W. *et al.* (Apr. 1994). “Nanoscale patterning and oxidation of H-passivated SI(100)-2×1 surfaces with an ultrahigh vacuum scanning tunneling microscope”. In: *Applied Physics Letters* 64.15, pp. 2010–2012. DOI: 10.1063/1.111722.

Mak, K. F. *et al.* (2014). “The Valley Hall effect in MoS2nbsp; transistors”. In: *Science* 344.6191, pp. 1489–1492. DOI: 10.1126/science.1250140.

Mak, Kin Fai *et al.* (2012). “Control of Valley polarization in monolayer Mos2 by Optical Helicity”. In: *Nature Nanotechnology* 7.8, pp. 494–498. DOI: 10.1038/nnano.2012.96.

Malmodin, Jens *et al.* (2023). “ICT sector electricity consumption and greenhouse gas emissions – 2020 outcome”. In: *SSRN Electronic Journal*. DOI: 10.2139/ssrn.4424264.

Mamin, H. *et al.* (1999). “High-density data storage based on the Atomic Force Microscope”. In: *Proceedings of the IEEE* 87.6, pp. 1014–1027. DOI: 10.1109/5.763314.

Mamin, H. J. and D. Rugar (1992). “Thermomechanical writing with an atomic force microscope tip”. In: *Applied Physics Letters* 61.8, pp. 1003–1005. DOI: 10.1063/1.108460.

Manfrinato, Vitor R. *et al.* (2013). “Resolution limits of electron-beam lithography toward the atomic scale”. In: *Nano Letters* 13.4, pp. 1555–1558. DOI: 10.1021/nl304715p.

Martin, Y. and H. K. Wickramasinghe (May 1987). “Magnetic Imaging by “‘force microscopy’” with 1000 Å resolution”. In: *Applied Physics Letters* 50.20, pp. 1455–1457. DOI: 10.1063/1.97800.

Martínez, Ramses V, Javier Martínez, and Ricardo Garcia (May 2010). “Silicon nanowire circuits fabricated by AFM oxidation nanolithography”. In: *Nanotechnology* 21.24, p. 245301. DOI: 10.1088/0957-4484/21/24/245301.

Meilan, Pablo F. and Mario Garavaglia (Dec. 1997). “Rayleigh resolution criterion for light sources of different spectral composition”. In: *Brazilian Journal of Physics* 27.4, pp. 638–643. DOI: 10.1590/s0103-97331997000400027.

Miccoli, I *et al.* (May 2015). "The 100th anniversary of the four-point probe technique: The role of probe geometries in isotropic and anisotropic systems". In: *Journal of Physics: Condensed Matter* 27.22, p. 223201. DOI: 10.1088/0953-8984/27/22/223201.

Mironov, V. L. *et al.* (Sept. 2009). "Magnetic force microscope tip-induced remagnetization of Copt nanodisks with Perpendicular anisotropy". In: *Journal of Applied Physics* 106.5. DOI: 10.1063/1.3202354.

Mitta, Sekhar Babu *et al.* (Nov. 2020). "Electrical characterization of 2D materials-based field-effect transistors". In: *2D Materials* 8.1, p. 012002. DOI: 10.1088/2053-1583/abc187.

Mojarad, N. *et al.* (2015). "Single-digit-resolution nanopatterning with extreme ultraviolet light for the 2.5 NM technology node and beyond". In: *Nanoscale* 7.9, pp. 4031–4037. DOI: 10.1039/c4nr07420c.

Moore, Gordon E. (Apr. 1965). "Cramming more components onto integrated circuits". In: *Electronics* 38.8.

Novoselov, K. S., A. K. Geim, *et al.* (Oct. 2004). "Electric field effect in atomically thin carbon films". In: *Science* 306.5696, pp. 666–669. DOI: 10.1126/science.1102896.

Novoselov, K. S., D. Jiang, *et al.* (July 2005). "Two-dimensional atomic crystals". In: *Proceedings of the National Academy of Sciences* 102.30, pp. 10451–10453. DOI: 10.1073/pnas.0502848102.

Ottaviano, L *et al.* (Sept. 2017). "Mechanical exfoliation and layer number identification of MOS2revisited". In: *2D Materials* 4.4, p. 045013. DOI: 10.1088/2053-1583/aa8764.

Oyabu, Noriaki *et al.* (Jan. 2005). "Lateral manipulation of single atoms at semiconductor surfaces using atomic force microscopy". In: *Nanotechnology* 16.3. DOI: 10.1088/0957-4484/16/3/021.

Paolucci, Valentina *et al.* (Sept. 2019). "Two-step exfoliation of WS2 for no2, H2 and humidity sensing applications". In: *Nanomaterials* 9.10, p. 1363. DOI: 10.3390/nano9101363.

Pavlova, T.V. *et al.* (Apr. 2020). "Local removal of silicon layers on Si(100)-2×1 with chlorine-resist STM lithography". In: *Applied Surface Science* 509, p. 145235. DOI: 10.1016/j.apsusc.2019.145235.

Piner, Richard D. *et al.* (Jan. 1999). ""Dip-pen" nanolithography". In: *Science* 283.5402, pp. 661–663. DOI: 10.1126/science.283.5402.661.

PolymerSolutions (2022). *TSPL resist solutions for Heidelberg's NanoFrazor*. URL: https://polymersol.com/tspl-resists.

Raja, Archana *et al.* (May 2017). "Coulomb engineering of the bandgap and excitons in two-dimensional materials". In: *Nature Communications* 8.1. DOI: 10.1038/ncomms15251.

Randall, John N. *et al.* (Oct. 2018). "Highly parallel scanning tunneling microscope based hydrogen depassivation lithography". In: *Journal of Vacuum Science amp; Technology B, Nanotechnology and Microelectronics: Materials, Processing, Measurement, and Phenomena* 36.6. DOI: 10.1116/1.5047939.

Rashidi, Mohammad, Jeremiah Croshaw, *et al.* (Mar. 2020). "Deep learning-guided surface characterization for autonomous hydrogen lithography". In: *Machine Learning: Science and Technology* 1.2, p. 025001. DOI: 10.1088/2632-2153/ab6d5e.

Rashidi, Mohammad, Wyatt Vine, *et al.* (Oct. 2018). "Initiating and Monitoring the Evolution of Single Electrons Within Atom-Defined Structures". In: *Phys. Rev. Lett.* 121 (16), p. 166801. DOI: 10.1103/PhysRevLett.121.166801. URL: https://link.aps.org/doi/10.1103/PhysRevLett.121.166801.

Ronse, Kurt (Mar. 2024). “Patterning infrastructure development for advanced EUV lithography: Continuing dimensional scaling through EUV lithography to support Moore’s law”. In: *IEEE Electron Devices Magazine* 2.1, pp. 35–44. DOI: 10.1109/med.2023.3336276.

Roos, Wouter H. (Jan. 2018). “AFM nanoindentation of protein shells, expanding the approach beyond viruses”. In: *Seminars in Cell amp; Developmental Biology* 73, pp. 145–152. DOI: 10.1016/j.semcdb.2017.07.044.

Rosenberger, Matthew R. *et al.* (Jan. 2019). “Quantum calligraphy: Writing single-photon emitters in a two-dimensional materials platform”. In: *ACS Nano* 13.1, pp. 904–912. DOI: 10.1021/acsnano.8b08730.

Russo, S. *et al.* (Feb. 2010). “Contact resistance in graphene-based devices”. In: *Physica E: Low-dimensional Systems and Nanostructures* 42.4, pp. 677–679. DOI: 10.1016/j.physe.2009.11.080.

Ryu, Yu Kyoung and Javier Martinez Rodrigo (2022). “Thermal scanning probe lithography”. In: *Scanning Probe Lithography*, pp. 85–102. DOI: 10.1201/9781003223610-7.

Ryu Cho, Yu Kyoung *et al.* (Nov. 2017). “Sub-10 nanometer feature size in silicon using thermal scanning probe lithography”. In: *ACS Nano* 11.12, pp. 11890–11897. DOI: 10.1021/acsnano.7b06307.

Saito, Yu *et al.* (2015a). “Superconductivity protected by spin–Valley locking in ion-gated mos2”. In: *Nature Physics* 12.2, pp. 144–149. DOI: 10.1038/nphys3580.

— (2015b). “Superconductivity protected by spin–Valley locking in ion-gated mos2”. In: *Nature Physics* 12.2, pp. 144–149. DOI: 10.1038/nphys3580.

Schumacher, H. W. *et al.* (Aug. 1999). “Nanomachining of mesoscopic electronic devices using an atomic force microscope”. In: *Applied Physics Letters* 75.8, pp. 1107–1109. DOI: 10.1063/1.124611.

Schwierz, Frank (May 2010). “Graphene transistors”. In: *Nature Nanotechnology* 5.7, pp. 487–496. DOI: 10.1038/nnano.2010.89.

Siao, M. D. *et al.* (Apr. 2018). “Two-dimensional electronic transport and surface electron accumulation in MOS2”. In: *Nature Communications* 9.1. DOI: 10.1038/s41467-018-03824-6.

Sugimoto, Yoshiaki *et al.* (Mar. 2007). “Mechanism for Room-Temperature Single-Atom Lateral Manipulations on Semiconductors using Dynamic Force Microscopy”. In: *Phys. Rev. Lett.* 98 (10), p. 106104. DOI: 10.1103/PhysRevLett.98.106104. URL: https://link.aps.org/doi/10.1103/PhysRevLett.98.106104.

Tennant, D. M. (1999). “Limits of conventional lithography”. In: *Nanotechnology*, pp. 161–205. DOI: 10.1007/978-1-4612-0531-9_4.

Ternes, Markus *et al.* (Feb. 2008). “The force needed to move an atom on a surface”. In: *Science* 319.5866, pp. 1066–1069. DOI: 10.1126/science.1150288.

UNEP (Dec. 2022). “Emissions Gap Report 2022”. In: *The Emissions Gap Report*. DOI: 10.18356/9789210023993.

Wang, Chuanshou *et al.* (2023). “Towards two-dimensional van der waals ferroelectrics”. In: *Nature Materials* 22.5, pp. 542–552. DOI: 10.1038/s41563-022-01422-y.

Wang, Joel I-Jan *et al.* (Feb. 2015). “Electronic Transport of Encapsulated Graphene and WSE2 devices fabricated by pick-up of prepatterned hbn”. In: *Nano Letters* 15.3, pp. 1898–1903. DOI: 10.1021/nl504750f.

Williams, C C. and H K. Wickramasinghe (1988). “Thermal and photothermal imaging on a sub 100 nanometer scale”. In: *SPIE Proceedings*. DOI: 10.1117/12.944530.

Williams, C.C. and H.K. Wickramasinghe (1986). “High resolution thermal microscopy”. In: *IEEE 1986 Ultrasonics Symposium*. DOI: 10.1109/ultsym.1986.198771.

Wolf, Heiko *et al.* (Nov. 2014). “Sub-20nm silicon patterning and metal lift-off using thermal scanning probe lithography”. In: *Journal of Vacuum Science amp; Technology B, Nanotechnology and Microelectronics: Materials, Processing, Measurement, and Phenomena* 33.2. DOI: 10.1116/1.4901413.

Wu, Chien-Ching *et al.* (Jan. 2010). “Protein immobilization on ni(ii) ion patterns prepared by microcontact printing and Dip-Pen Nanolithography”. In: *ACS Nano* 4.2, pp. 1083–1091. DOI: 10.1021/nn901270c.

Xi, Xiaoxiang *et al.* (2015). “Ising pairing in superconducting nbse2 atomicnbsp;layers”. In: *Nature Physics* 12.2, pp. 139–143. DOI: 10.1038/nphys3538.

Xiao, Di *et al.* (2012). “Coupled spin and valley physics in monolayers of MoS2 and other group-VI dichalcogenides.” In: *Physical Review Letters* 108.19. DOI: 10.1103/physrevlett.108.196802.

Xu, Yang *et al.* (May 2016). “Contacts between two- and three-dimensional materials: Ohmic, Schottky, and p–n heterojunctions”. In: *ACS Nano* 10.5, pp. 4895–4919. DOI: 10.1021/acsnano.6b01842.

Yamachika, R. *et al.* (Apr. 2004). “Controlled atomic doping of a single C60 molecule”. In: *Science* 304.5668, pp. 281–284. DOI: 10.1126/science.1095069.

Young, Russell, John Ward, and Fredric Scire (1972). “The topografiner: An instrument for measuring surface microtopography”. In: *Review of Scientific Instruments* 43.7, pp. 999–1011. DOI: 10.1063/1.1685846.

Zafar, Amina *et al.* (Nov. 2016). “Probing the intrinsic optical quality of CVD grown MOS2”. In: *Nano Research* 10.5, pp. 1608–1617. DOI: 10.1007/s12274-016-1319-z.

Zhang, Yuning *et al.* (Apr. 2019). “Nanopore formation via tip-controlled local breakdown using an atomic force microscope”. In: *Small Methods* 3.7. DOI: 10.1002/smtd.201900147.

Zheng, Xiaorui *et al.* (Jan. 2019). “Patterning metal contacts on monolayer MOS2 with vanishing Schottky barriers using thermal nanolithography”. In: *Nature Electronics* 2.1, pp. 17–25. DOI: 10.1038/s41928-018-0191-0.

Zhou, Xiaozhu *et al.* (Mar. 2013). “Locally altering the electronic properties of graphene by nanoscopically doping it with Rhodamine 6G”. In: *Nano Letters* 13.4, pp. 1616–1621. DOI: 10.1021/nl400043q.

Appendix A - Supplementary Information

A.1 Airy Disk Python Simulation

Below is the python code used to compute both the 2D and 3D Airy disk simulations seen in the introduction.

```
import numpy as np
import matplotlib.pyplot as plt
from scipy.special import j1
from matplotlib.colors import LogNorm


# Define the Airy disk function based on the Bessel
def airy(r, beta):
    if r == 0:
        return (1 - np.exp(-(2/beta**2))) / (np.pi * beta**2)
    else:
        return ((1 - np.exp(-(2/beta**2))) * (j1((2 * np.pi * r) /
                                               beta)**2)) / (np.pi * r**2
                                                * beta**2)

# Generate the values for r
r = np.linspace(0, 1.5, 1000)

# Calculate the Airy function values
```

```
beta = 1
z = np.array([airy(ri, beta) for ri in r])

# Normalize the irradiance values
z = z / np.max(z)

# Create the 3D revolution plot
fig = plt.figure(figsize=(14, 6))

ax1 = fig.add_subplot(121, projection='3d')

# Generate the meshgrid for the revolution plot
theta = np.linspace(0, 2 * np.pi, 500)
r, theta = np.meshgrid(2 * r, theta)
x = r * np.cos(theta)
y = r * np.sin(theta)
z = np.array([airy(ri, beta) for ri in r.flatten()]).reshape(r.shape)

# Normalize the irradiance values again for the 3D plot
z = z / np.max(z)

shift = 0.5  # Shift by 0.5 microns
z1 = np.array([airy(np.sqrt((xi - shift / 2)**2 + (yi)**2), beta) for
                                    xi, yi in zip(x.flatten(), y.
                                   flatten())]).reshape(x.shape)
z2 = np.array([airy(np.sqrt((xi + shift / 2)**2 + (yi)**2), beta) for
                                    xi, yi in zip(x.flatten(), y.
                                   flatten())]).reshape(x.shape)

# Normalize the shifted irradiance values
z1 = z1 / np.max(z1)
z2 = z2 / np.max(z2)
z_sum = z1 + z2
```

```
# Plot the summed PSF in 3D
surf = ax1.plot_surface(x, y, z_sum, cmap='jet', edgecolor='none',
                                    alpha=0.95,  norm=LogNorm(vmin=5e-
                                    3, vmax=1))

# Add grid and axes
ax1.grid(True)
ax1.set_xlabel('X (microns)')
ax1.set_ylabel('Y (microns)')
ax1.set_zlabel('Irradiance (relative)')
ax1.set_title('Two Airy Disks: Point Spread Functions (PSF)')

# Set plot properties
ax1.set_box_aspect([1, 1, 1])  # Aspect ratio is 1:1:1

# Add color bar
fig.colorbar(surf, ax=ax1, shrink=0.5, aspect=5, label='Irradiance (
                                    relative)')

# Plot the summed PSF in 2D
ax2 = fig.add_subplot(122)
c = ax2.pcolormesh(x, y, z_sum, cmap='jet', shading='auto', norm=
                                    LogNorm(vmin=5e-3, vmax=1)) #Log
                                    norm the smaller values to be
                                    visible in 2D plot
fig.colorbar(c, ax=ax2, shrink=0.5, aspect=5, label='Irradiance (
                                    relative)')
ax2.grid(False)

plt.tight_layout()
plt.show()
```

A.2 Illustration of Over-development Flaw

Below is an illustration of what may occur during excessive over-development of the PMGI. This image serves to visualize a plausible explanation for what occurred in Figure 2.8 (c-e). This issue was resolved by placing the sample in a sonicator bath to break the overcoat from the electrodes. The figure is not drawn to scale. The figure omits the adhesive layer under the gold for simplicity.

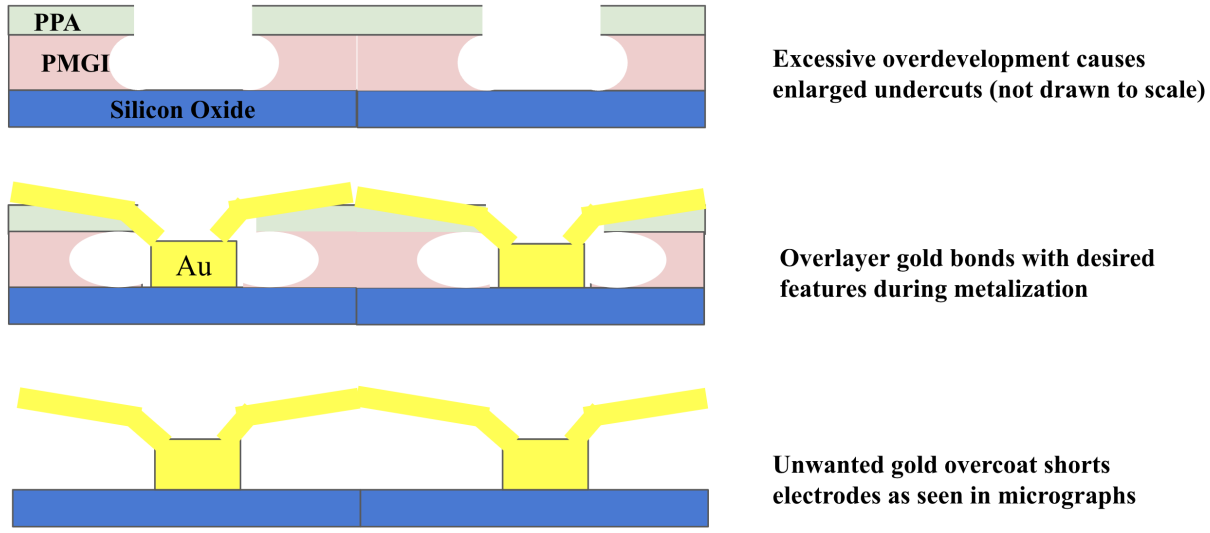

A.3 Raman Spectra, Residuals, and Deconvolution

This first graph provides the deconvolved spectra for the mechanically exfoliated WS_2 at the A_{1g} (Γ) modes for various layers on the flake. Residual plots and fitting parameters for both 3.3(c and d) can be seen below.

The plot below overlaps both Raman spectra for the "naked" mechanically exfoliated flake as well as the one with four electrodes attached to it in a van der Pauw configuration. Micrographs of these samples can be observed in Figure 3.3(a and b).

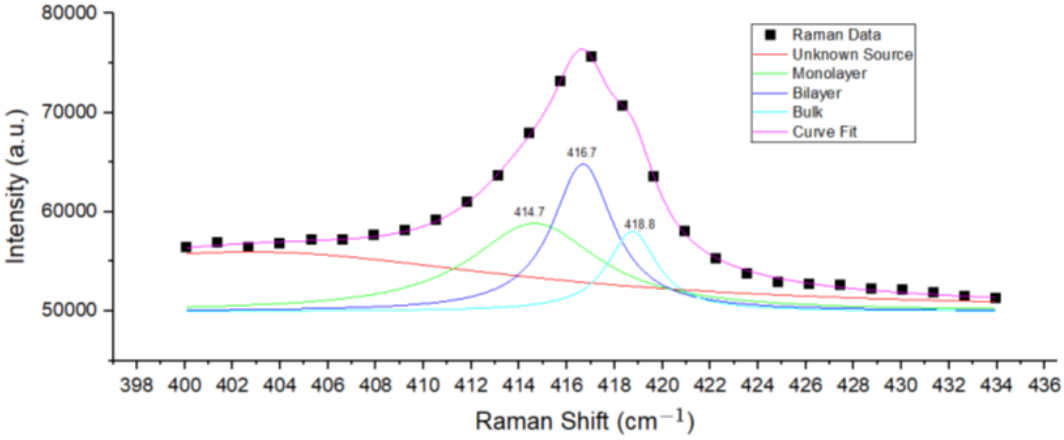
Raman Data
Unknown Source
Monolayer
Bilayer
Bulk
Curve Fit
416.7
414.7
418.8
Intensity (a.u.)
Raman Shift (cm^{-1})

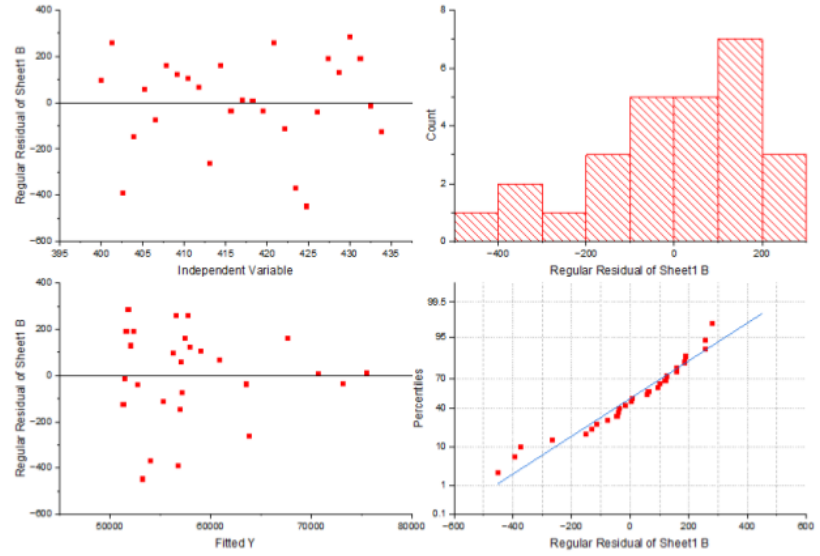
Regular Residual of Sheet1 B
Independent Variable
Count
Regular Residual of Sheet1 B
Regular Residual of Sheet1 B
Fitted Y
Percentiles
Regular Residual of Sheet1 B

Model	Lorentz			
Equation	y = y0 + (2*A/pi)*(w/(4*(x-xc)^2 + w^2))			
Plot	Peak1(B)	Peak2(B)	Peak3(B)	Peak4(B)
y0	49970.56589 ± 1290.45856	49970.56589 ± 1290.45856	49970.56589 ± 1290.45856	49970.56589 ± 1290.45856
xc	402.7103 ± 3.02146	414.64137 ± 8.95192	416.66881 ± 1.45582	418.74435 ± 2.04727
w	27.32337 ± 20.16935	6.61093 ± 4.06686	3.10881 ± 18.06175	2.5385 ± 3.12133
A	257403.48317 ± 292022.01121	91946.21877 ± 615714.72198	72488.49062 ± 721128.73144	32146.91299 ± 190753.77939
Reduced Chi-Sqr	72873.85075			
R-Square (COD)	0.99913			
Adj. R-Square	0.99839			

Model	Lorentz				
Equation	y = y0 + (2*A/pi)*(w/(4*(x-xc)^2 + w^2))				
Plot	Peak1(B)	Peak2(B)	Peak3(B)	Peak4(B)	Peak5(B)
y0	45659.37361 ± 2960.87414	45659.37361 ± 2960.87414	45659.37361 ± 2960.87414	45659.37361 ± 2960.87414	45659.37361 ± 2960.87414
xc	268.90511 ± 6.93861	298.98368 ± 1.00474	322.48397 ± 0.6134	342.909 ± 1.88036	351.19012 ± 0.30758
w	46.1036 ± 48.32206	23.35894 ± 6.49836	17.47728 ± 3.01395	17.30582 ± 4.81832	11.8255 ± 0.96349
A	2095537.0998 ± 2634522.36488	1611379.55988 ± 857394.57087	1399817.53519 ± 325013.02345	1817756.28642 ± 1024895.12735	3428878.08443 ± 714069.8528
Reduced Chi-Sqr	2.17672E7				
R-Square (COD)	0.99277				
Adj. R-Square	0.99126				

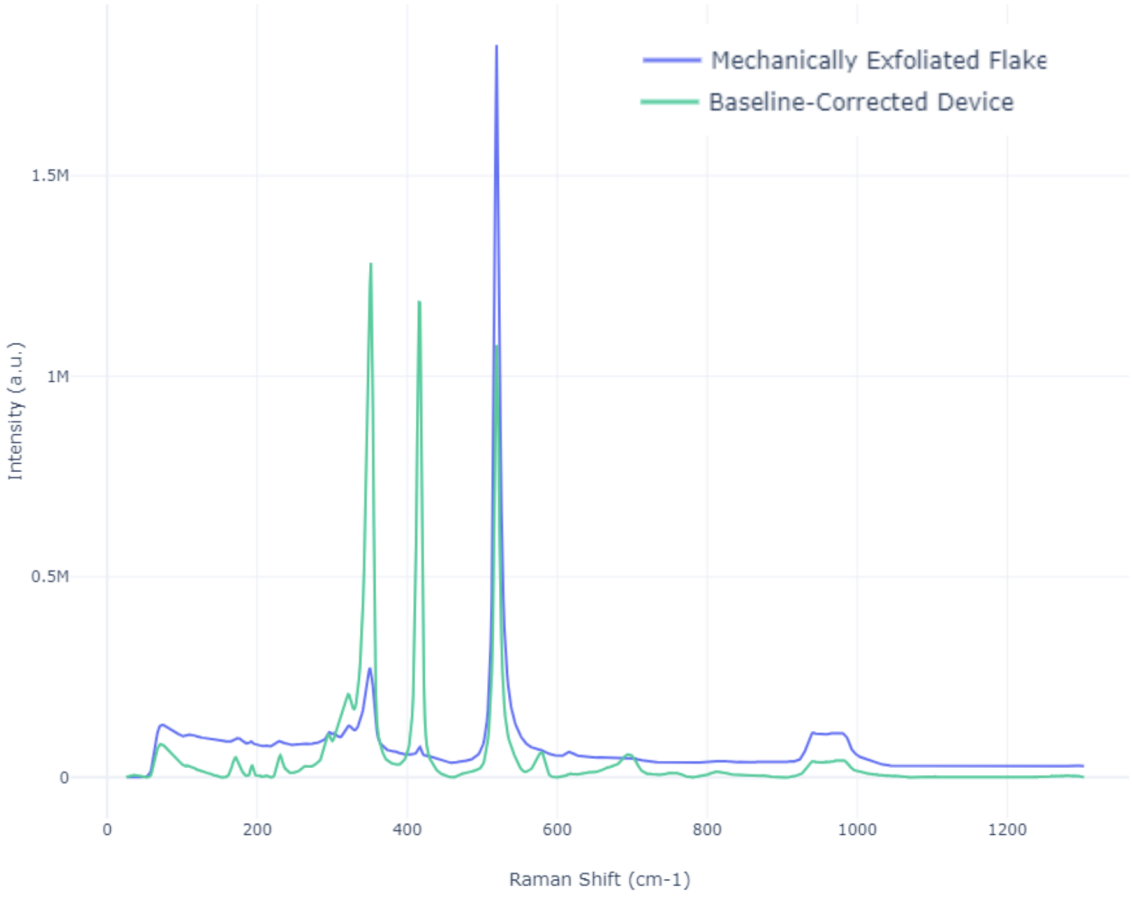
Mechanically Exfoliated Flake
Baseline-Corrected Device
1.5M
1M
0.5M
0
Intensity (a.u.)
0
200
400
600
800
1000
1200
Raman Shift (cm-1)

A.4 Topographic Histograms and Curve Fits

Below are the histogram curves and Lorentzian fits of the masked regions from the TM-AFM height data as well as supplementary information regarding moment-based, order-based, and hybrid statistical quantities calculated in the Gwyddion software. The masked regions can be seen as a unique shade of red on the AM-AFM topography scans in the insets of each relevant graphs. All operations received the same Gwyddion image preprocessing procedure as previously discussed in the TM-AFM section.

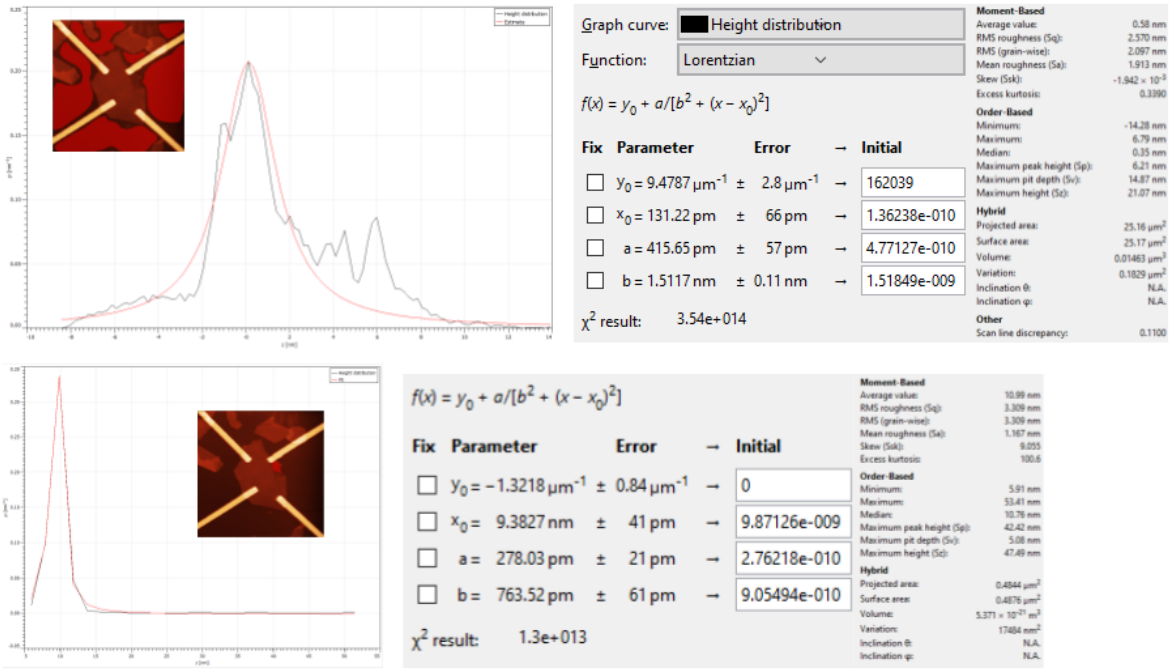

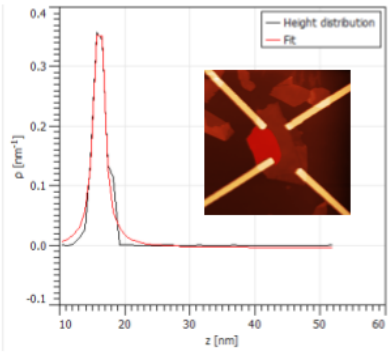

Graph curve: Height distribution

Function: Lorentzian

$f(x) = y_0 + a/[b^2 + (x - x_0)^2]$

Fix	Parameter		Error	→	Initial
☐	y_0 = −3.5285 µm⁻¹	±	2.0 µm⁻¹	→	0
☐	x_0 = 16.111 nm	±	24 pm	→	1.56728e-008
☐	a = 336.56 pm	±	30 pm	→	2.72506e-010
☐	b = 868.54 pm	±	50 pm	→	8.74317e-010

χ^2 result: 1.46e+014

Moment-Based

Average value:	16.71 nm
RMS roughness (Sq):	1.458 nm
RMS (grain-wise):	1.458 nm
Mean roughness (Sa):	0.894 nm
Skew (Ssk):	7.656
Excess kurtosis:	165.0

Order-Based

Minimum:	10.40 nm
Maximum:	52.59 nm
Median:	16.60 nm
Maximum peak height (Sp):	35.89 nm
Maximum pit depth (Sv):	6.31 nm
Maximum height (Sz):	42.20 nm

Hybrid

Projected area:	3.931 µm²
Surface area:	3.937 µm²
Volume:	0.06577 µm³
Variation:	57845 nm²
Inclination θ:	N.A.
Inclination φ:	N.A.

Other

Scan line discrepancy:	0.06775

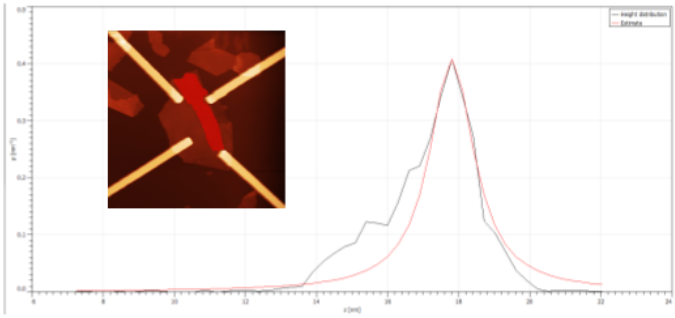

Graph curve: Height distribution

Function: Lorentzian

$f(x) = y_0 + a/[b^2 + (x - x_0)^2]$

Fix	Parameter		Error	→	Initial
☐	y_0 = 0.0000 m⁻¹	±		→	0
☐	x_0 = 17.641 nm	±		→	1.78019e-008
☐	a = 354.28 pm	±		→	2.38389e-010
☐	b = 963.04 pm	±		→	7.64204e-010

χ^2 result:

Correlation Matrix

Range: 7.245 to 22.025 nm

Moment-Based

Average value:	17.29 nm
RMS roughness (Sq):	1.439 nm
RMS (grain-wise):	1.439 nm
Mean roughness (Sa):	1.109 nm
Skew (Ssk):	-1.038
Excess kurtosis:	3.165

Order-Based

Minimum:	7.25 nm
Maximum:	22.33 nm
Median:	17.57 nm
Maximum peak height (Sp):	5.04 nm
Maximum pit depth (Sv):	10.04 nm
Maximum height (Sz):	15.08 nm

Hybrid

Projected area:	4.397 µm²
Surface area:	4.398 µm²
Volume:	0.07598 µm³
Variation:	53076 nm²
Inclination θ:	N.A.
Inclination φ:	N.A.

Other

Scan line discrepancy:	27.96 × 10⁻³

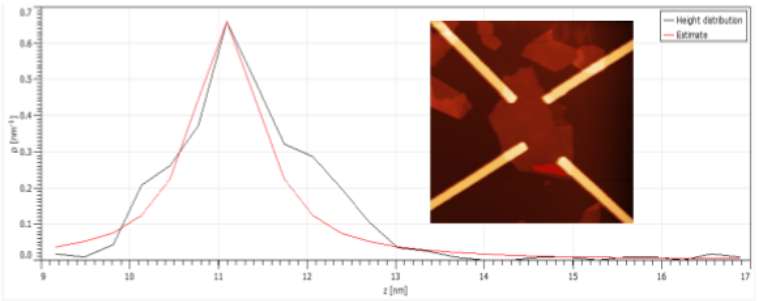

Graph curve: Height distribution

Function: Lorentzian

$f(x) = y_0 + a/[b^2 + (x - x_0)^2]$

Fix	Parameter		Error	→	Initial
☐	y_0 = 0.0000 m⁻¹	±		→	0
☐	x_0 = 11.196 nm	±		→	1.10951e-008
☐	a = 229.49 pm	±		→	1.41452e-010
☐	b = 608.38 pm	±		→	4.629e-010

χ^2 result:

Correlation Matrix

Range: 9.165 to 16.884 nm

Moment-Based

Average value:	11.55 nm
RMS roughness (Sq):	983.6 pm
RMS (grain-wise):	983.6 pm
Mean roughness (Sa):	676.0 pm
Skew (Ssk):	1.987
Excess kurtosis:	8.363

Order-Based

Minimum:	9.17 nm
Maximum:	17.21 nm
Median:	11.41 nm
Maximum peak height (Sp):	5.65 nm
Maximum pit depth (Sv):	2.39 nm
Maximum height (Sz):	8.04 nm

Hybrid

Projected area:	0.5506 µm²
Surface area:	0.5510 µm²
Volume:	6.393 × 10⁻²¹ m³
Variation:	11824 nm²
Inclination θ:	N.A.
Inclination φ:	N.A.

Other

Scan line discrepancy:	0.05277

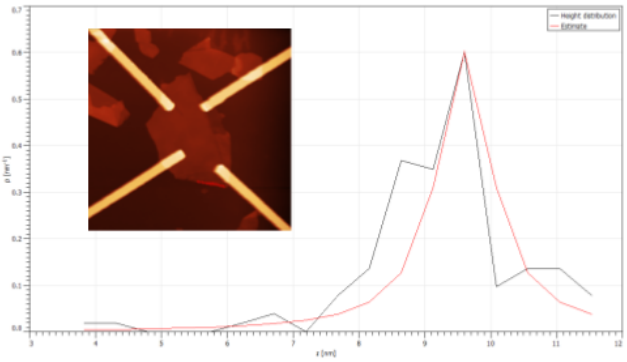

Graph curve: Height distribution

Function: Lorentzian

$f(x) = y_0 + a/[b^2 + (x - x_0)^2]$

Fix	Parameter		Error	→	Initial
☐	y_0 = 0.0000 m⁻¹	±		→	0
☐	x_0 = 9.3903 nm	±		→	9.60317e-009
☐	a = 231.12 pm	±		→	1.49191e-010
☐	b = 652.37 pm	±		→	4.97993e-010

χ^2 result:

Correlation Matrix

Range: 3.824 to 11.530 nm

Moment-Based

Average value:	9.48 nm
RMS roughness (Sq):	1.259 nm
RMS (grain-wise):	1.259 nm
Mean roughness (Sa):	0.870 nm
Skew (Ssk):	-1.306
Excess kurtosis:	4.591

Order-Based

Minimum:	3.82 nm
Maximum:	12.01 nm
Median:	9.62 nm
Maximum peak height (Sp):	2.53 nm
Maximum pit depth (Sv):	5.65 nm
Maximum height (Sz):	8.19 nm

Hybrid

Projected area:	0.1646 µm²
Surface area:	0.1649 µm²
Volume:	1.530 × 10⁻²¹ m³
Variation:	7167 nm²
Inclination θ:	N.A.
Inclination φ:	N.A.

Other

Scan line discrepancy:	0.1715

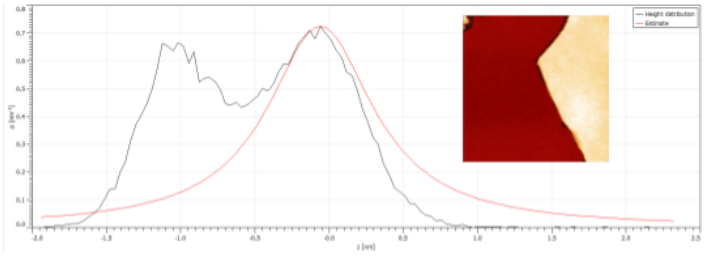

Graph curve: Height distribution

Function: Lorentzian

$f(x) = y_0 + a/[b^2 + (x - x_0)^2]$

Fix	Parameter		Error	→	Initial
☐	y_0 = 0.0000 m^{-1}	±		→	0
☐	x_0 = −462.21 pm	±		→	-5.91156e-011
☐	a = 327.00 pm	±		→	1.37459e-010
☐	b = 711.96 pm	±		→	4.3544e-010

χ^2 result:

Moment-Based

Average value:	-0.470 nm
RMS roughness (Sq):	538.1 pm
RMS (grain-wise):	538.1 pm
Mean roughness (Sa):	484.3 pm
Skew (Ssk):	5.751×10^{-3}
Excess kurtosis:	-0.8826

Order-Based

Minimum:	-1.939 nm
Maximum:	2.353 nm
Median:	-0.427 nm
Maximum peak height (Sp):	2.823 nm
Maximum pit depth (Sv):	1.470 nm
Maximum height (Sz):	4.293 nm

Hybrid

Projected area:	1.737 μm^2
Surface area:	1.738 μm^2
Volume:	-814.3×10^{-18} m^3
Variation:	55033 nm^2
Inclination θ:	N.A.
Inclination φ:	N.A.

Other

Scan line discrepancy:	0.2062

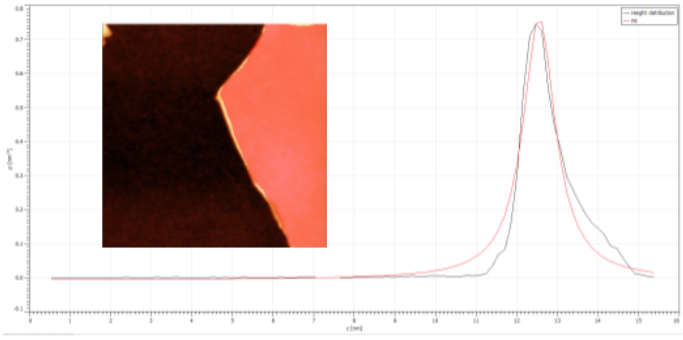

Graph curve: Height distribution

Function: Lorentzian

$f(x) = y_0 + a/[b^2 + (x - x_0)^2]$

Fix	Parameter		Error	→	Initial
☐	y_0 = −6.6493 μm^{-1}	±	4.2 μm^{-1}	→	0
☐	x_0 = 12.549 nm	±	14 pm	→	1.24669e-008
☐	a = 181.16 pm	±	12 pm	→	1.33267e-010
☐	b = 483.58 pm	±	19 pm	→	4.22988e-010

χ^2 result: 1.19e+015

Moment-Based

Average value:	12.84 nm
RMS roughness (Sq):	825.2 pm
RMS (grain-wise):	825.2 pm
Mean roughness (Sa):	573.7 pm
Skew (Ssk):	-1.959
Excess kurtosis:	23.68

Order-Based

Minimum:	0.55 nm
Maximum:	15.52 nm
Median:	12.73 nm
Maximum peak height (Sp):	2.68 nm
Maximum pit depth (Sv):	12.29 nm
Maximum height (Sz):	14.97 nm

Hybrid

Projected area:	0.9353 μm^2
Surface area:	0.9367 μm^2
Volume:	0.01201 μm^3
Variation:	33571 nm^2
Inclination θ:	N.A.
Inclination φ:	N.A.

Other

Scan line discrepancy:	11.52×10^{-3}